Monthly Notices of the ROYAL ASTRONOMICAL SOCIETY

MNRAS **505,** 5283–5300 (2021) https://doi.org/10.1093/mnras/stab1653
Advance Access publication 2021 June 10

Fundamental differences in the radio properties of red and blue quasars: kiloparsec-scale structures revealed by e-MERLIN

D. J. Rosario,[1]★ D. M. Alexander,[1] J. Moldon,[2,3] L. Klindt ,[1] A. P. Thomson,[3] L. Morabito ,[1] V. A. Fawcett[1] and C. M. Harrison [4]

[1]*Centre for Extragalactic Astronomy, Department of Physics, Durham University, South Road, Durham DH1 3LE, UK*
[2]*Instituto de Astrofísica de Andalucía (IAA, CSIC), Glorieta de las Astronomía, s/n, E-18008 Granada, Spain*
[3]*Jodrell Bank Centre for Astrophysics, School of Physics and Astronomy, University of Manchester, Manchester M13 9PL, UK*
[4]*School of Mathematics, Statistics and Physics, Newcastle University, Newcastle Upon Tyne NE1 7RU, UK*

Accepted 2021 June 4. Received 2021 June 4; in original form 2021 March 9

ABSTRACT

Red quasi-stellar objects (QSOs) are a subset of the quasar population with colours consistent with reddening due to intervening dust. Recent work has demonstrated that red QSOs show special radio properties that fundamentally distinguish them from normal blue QSOs, specifically a higher incidence of low-power radio emission (1.4 GHz luminosities $L_{1.4} \approx 10^{25}$–10^{27} W Hz^{-1}) that is physically compact when imaged by arcsecond-resolution radio surveys such as FIRST. In this work, we present e-MERLIN imaging of a set of intermediate-redshift ($1.0 < z < 1.55$), luminous (bolometric luminosities $L_{\rm bol} \approx 10^{46}$–$10^{47}$ erg s^{-1}) red and normal QSOs carefully selected to have radio properties that span the range over which red QSOs show the most divergence from the general population. With an angular resolution 25× better than FIRST, we resolve structures within the host galaxies of these QSOs (>2 kpc). We report a statistically significant difference in the incidence of extended kpc-scale emission in red QSOs. From an analysis of the radio size distributions of the sample, we find that the excess radio emission in red QSOs can be attributed to structures that are confined to galaxy scales (<10 kpc), while we confirm previous results that red and normal QSOs have similar incidences of radio jets and lobes on circumgalactic or larger scales (>10 kpc). Our results indicate that the primary mechanism that generates the enhanced radio emission in red QSOs is not directly connected with the nuclear engine or accretion disc, but is likely to arise from extended components such as AGN-driven jets or winds.

Key words: methods: observational – techniques: interferometric – galaxies: jets – quasars: individual – radio continuum: galaxies.

1 INTRODUCTION

Quasi-stellar objects (QSOs) are the luminous tail of the population of active galactic nuclei (AGNs) and account for a substantial part of the cosmic mass growth in supermassive black holes (SMBHs). Their distinctive features, high optical luminosities and clear spectroscopic signatures of broad emission lines, are the manifestation of an unimpaired line-of-sight view towards the central accretion engine and its immediate environment. Due to their bright optical emission and relative ease of identification, QSOs are valuable signposts of the locations at which the co-evolutionary connections between galaxies and SMBHs are put into place. Therefore, a thorough understanding of the processes by which QSOs regulate their own growth and influence their host galaxies is valuable for our developing picture of the evolution of SMBH scaling relations, and for the evolution of massive galaxies as a whole.

The majority of QSOs have blue ultraviolet-to-optical colours consistent with direct thermal emission from an AGN accretion disc peaking in the extreme ultraviolet (effective temperatures $\sim 10^5$ K). Large spectroscopic surveys, such as the Sloan Digital Sky Survey (SDSS), have identified a subset of QSOs that scatter to much redder colours (e.g. Richards et al. 2003). In this work, we will use the abbreviation 'rQSOs' to refer to red QSOs.

There are a number of possible reasons for the red colours of rQSOs, such as intrinsically cooler accretion discs, host galaxy light, or Doppler-boosted synchrotron emission (e.g. Benn et al. 1998; Francis et al. 2001; Young, Elvis & Risaliti 2008), but the vast majority of luminous rQSOs are reddened by intervening dust (Richards et al. 2003; Glikman et al. 2004, 2012; Rose et al. 2013; Kim & Im 2018; Klindt et al. 2019).

As the colours of rQSOs are not as distinct as those of normal (blue) QSOs, they can be difficult to separate photometrically from stars and compact galaxies. In the early days of rQSO research, strong radio emission, a hallmark of some classes of AGN, was widely used to select and study this subpopulation (Webster et al. 1995; Ivezić et al. 2002; White et al. 2003; Glikman et al. 2004). Over time, growing evidence suggested that redder QSOs were associated with a high fraction of radio sources (Richards et al. 2003; White et al. 2007; Georgakakis et al. 2009; Tsai & Hwang 2017), though clear conclusions were elusive due to the complex selection effects that were built into the selection of rQSOs, including those related to radio emission itself (e.g. Richards et al. 2002).

In order to make progress in this area, our team has recently undertaken a careful and controlled study of the radio properties of rQSOs. In a pioneering paper, Klindt et al. (2019) undertook a

★ E-mail: david.rosario@durham.ac.uk

controlled study of QSOs selected from the SDSS and examined their incidence and morphologies using data from the Faint Images of the Radio Sky at Twenty centimetres survey (FIRST; Becker, White & Helfand 1995; Helfand, White & Becker 2015). We found a much higher detection rate of radio sources among rQSOs compared to equally luminous normal QSOs at the same redshifts. This result is attributable to a substantial excess of compact radio sources among rQSOs, with relatively low radio powers ($L_{1.4} < 10^{27}$ W Hz^{-1}, where $L_{1.4}$ is the integrated rest-frame 1.4 GHz radio luminosity of a radio source). Taking a similar strategy, Rosario et al. (2020) and Fawcett et al. (2020) confirmed the results of Klindt et al. (2019) at regimes of fainter optical and radio luminosities, different radio frequencies, and using higher resolution radio images.

Our various studies clearly demonstrate that rQSOs have distinct radio properties that cannot be easily explained by varying reddening over a parent population of normal QSOs. The chief conclusion is that rQSOs sustain an excess population of compact radio sources, with radio sizes smaller than the FIRST survey beamsize (5 arcsec; $\approx$40 kpc at $z \sim 1$), and with intermediate radio loudness. In this fashion, rQSOs are fundamentally different from normal QSOs, and their properties suggest a deep connection between the dust that reddens them and their radio emission mechanisms.

FIRST covers a large area of sky, which enables an accurate statistical assessment of the radio-detection statistics for SDSS QSOs. The angular resolution of FIRST marks a large improvement over most earlier radio surveys, but it offers only limited capabilities for the study of distant QSOs. In particular, over the important redshift interval of $1 < z < 3$ that marks the epochs at which most SMBH growth occurs, reliance on radio imaging with resolutions of a few arcseconds restricts studies to scales $\gtrsim$10 kpc, larger than the stellar sizes of the massive galaxies that host QSOs (e.g. van der Wel et al. 2014). Since interstellar reddening requires modest columns of gas and dust that are generally only available within galaxies, a clearer understanding of the nature of the radio sources in rQSOs requires radio observations with spatial resolutions of a few kpcs or lower.

First steps towards a higher resolution study were undertaken by Fawcett et al. (2020). Using images from the 1.4 GHz VLA/Stripe82 survey, we demonstrated that rQSOs show a slight excess of radio sources with sizes that were close to the resolution limit ($\approx$1.8 arcsec; $\approx$15 kpc at $z \sim 1$). This cemented the notion that the key to understanding the rQSO phenomenon lies at even smaller scales, well within the realm of the QSO hosts themselves.

Here, we present e-MERLIN observations of rQSOs and cQSOs with the express aim of understanding their morphologies and radio properties on scales of a few kpcs. Our study is designed to identify whether the peculiar morphological properties of rQSOs extend down to galaxy scales much smaller than those probed by FIRST. In Section 2, after a discussion of the sample and ancillary data, we describe the new e-MERLIN observations, their reduction, and the processing we have undertaken to characterize radio structure from the final images. In Section 3, we lay out our key measurements and results, and discuss their implications in Section 4 for the incidence, origin, and evolution of kpc-scale radio structure in QSOs. We summarize our conclusions in Section 5.

Throughout this work, we assume a concordance cosmology (Planck Collaboration XIII 2016) and implement it in our calculations using software built into the ASTROPY COSMOLOGY module.

2 DATA AND METHODS

The QSOs in this study are selected from the SDSS QSO catalogue based on their properties in the SDSS and FIRST surveys. We describe their selection and general features below, followed by a detailed treatment of their e-MERLIN observations and analysis.

2.1 SDSS colour-selected QSOs

2.1.1 Sample selection

We selected our targets for e-MERLIN imaging from the primary sample defined in Klindt et al. (2019). Starting from the SDSS DR7 catalogue of QSOs (Schneider et al. 2010), Klindt et al. (2019) applied a set of criteria to minimize the complications of selection biases and allow a refined comparative framework for their investigation into rQSOs. These involved: (1) the use of the UNIFORM_TARGET flag, (2) the exclusion of pure radio-selected QSOs, (3) a required detection in the *WISE W1*, *W2*, and *W3* bands (3.5, 4.6, and 12 μm, respectively) to allow the characterization of the accretion power of the AGN, and (4) the restriction to an upper redshift of $z = 2.4$ to ensure that the colour selection of QSOs was not affected by the Lyman break. Following Klindt et al. (2019), we will refer to this pre-selected subset of the DR7 QSO catalogue as the 'parent sample'.

At the accretion luminosities typical of high-redshift QSOs from the SDSS, the rest-frame mid-infrared (MIR) is dominated by emission from nuclear dust heated directly by the AGN. Since the MIR is negligibly affected by even moderate levels of dust extinction, MIR luminosities serve as a good measure of the nuclear power of these QSOs. From the *WISE* photometry available, by construction, for the entire parent sample, we estimate the rest-frame 6 μm luminosity ($L_{6\mu m}$) through a log-linear extrapolation of the *WISE W2* and *W3* fluxes, following the method described in Klindt et al. (2019) and used by other papers in this series.

Klindt et al. (2019) split QSOs from the parent sample into colour-selected categories based on their observed-frame SDSS $g - i$ colour distributions as a function of redshift. After grouping the parent sample into redshift-sorted bins of 1000 QSOs, they identified rQSOs as those that lie in the upper 10th percentile of the $g - i$ colour distribution in a bin. The rQSOs targeted with eMERLIN are a subset of the rQSOs defined by Klindt et al. (2019).

For our control sample of 'normal' QSOs (henceforth, cQSOs), we identify the 50 per cent of QSOs that lie about the median colour in the aforementioned redshift-sorted bins. This approach differs from Klindt et al. (2019), who only use the 10 per cent median to define their control sample. Our main motivation for implementing an expanded colour definition of the control sample was to allow more target choices after selection constraints on radio morphology and redshift, luminosity matching requirements, and e-MERLIN observability restrictions (see below). We are able to relax the colour criteria for cQSOs because Klindt et al. (2019) clearly demonstrated that the FIRST radio properties of blue QSOs do not differ significantly across the full range of colours shown by this population, implying that both 10 per cent and 50 per cent median cQSOs have indistinguishable radio properties. This has been verified in more recent work (Fawcett et al. 2020; Rosario et al. 2020), in which a 50 per cent median control sample, similar to the selection used in this paper, showed differences in radio properties to rQSOs that are consistent with a 10 per cent control.

A final selection requirement is that of radio compactness, since this is the morphological class in which the largest differences were found between red and normal QSOs. We identified compact radio sources through visual inspection of images from the FIRST radio survey following the methodology laid out in Klindt et al. (2019). In

Table 1. Key properties of the e-MERLIN targets.

SDSS identifier (1)	RA (deg) (2)	Dec. (deg) (3)	Redshift (4)	$L_{6\mu m}$ (5)	$L_{1.4}$ (6)
Red QSOs					
SDSSJ082314.71+560948.9	125.811 264	56.163 62	1.4433	45.12	26.03
SDSSJ082837.75+273136.9	127.157 333	27.526 92	1.4846	45.39	25.86
SDSSJ094615.01+254842.0	146.562 533	25.811 70	1.1940	45.78	25.91
SDSSJ095114.35+525316.7	147.809 845	52.887 96	1.4270	45.89	26.35
SDSSJ100713.68+285348.4	151.806 977	28.896 78	1.0470	46.08	25.86
SDSSJ105705.15+311907.8	164.271 484	31.318 83	1.3282	45.74	26.33
SDSSJ112220.45+312440.9	170.585 218	31.411 39	1.4534	45.74	26.37
SDSSJ114046.80+441609.8	175.195 022	44.269 39	1.4086	45.34	26.18
SDSSJ115313.06+565126.3	178.304 452	56.857 29	1.2014	45.84	26.49
SDSSJ115924.05+215103.0	179.850 216	21.850 83	1.0461	45.37	25.75
SDSSJ120201.91+631759.4	180.508 038	63.299 84	1.4806	45.42	25.93
SDSSJ121101.81+222106.7	182.757 562	22.351 88	1.2994	45.99	25.79
SDSSJ125146.34+431729.7	192.943 066	43.291 58	1.4527	45.27	26.40
SDSSJ131556.37+201701.6	198.984 945	20.283 78	1.4296	45.80	25.94
SDSSJ132304.23+394855.0	200.767 645	39.815 29	1.2797	45.48	26.12
SDSSJ134236.96+432632.1	205.653 994	43.442 24	1.0426	45.54	26.31
SDSSJ141053.19+401618.5	212.721 690	40.271 83	1.0425	44.94	25.87
SDSSJ153133.53+452841.6	232.889 728	45.478 22	1.0221	45.46	25.69
SDSSJ153555.27+243428.6	233.980 322	24.574 61	1.0779	45.43	25.97
Control QSOs					
SDSSJ074815.44+220059.4	117.064 346	22.016 52	1.0594	46.02	25.89
SDSSJ100318.93+272734.3	150.828 904	27.459 56	1.2893	45.85	25.95
SDSSJ101935.22+281738.9	154.896 733	28.294 16	1.0136	45.47	26.16
SDSSJ103850.89+415512.7	159.712 031	41.920 19	1.4678	45.99	25.97
SDSSJ104240.11+483403.4	160.667 146	48.567 62	1.0375	45.54	26.15
SDSSJ104620.18+342708.4	161.584 121	34.452 34	1.1964	45.75	26.59
SDSSJ105736.17+331545.9	164.400 726	33.262 76	1.4658	45.31	25.78
SDSSJ110352.48+584923.5	165.968 689	58.823 19	1.3300	45.63	25.95
SDSSJ120335.39+451049.5	180.897 481	45.180 43	1.0760	45.32	26.44
SDSSJ122221.37+372335.8	185.589 086	37.393 30	1.2647	45.31	26.11
SDSSJ130433.42+320635.5	196.139 280	32.109 89	1.3368	45.68	26.17
SDSSJ141027.58+221702.6	212.614 950	22.284 06	1.4181	45.47	26.59
SDSSJ142824.76+291606.7	217.103 202	29.268 56	1.0365	45.21	26.44
SDSSJ143249.54+292505.7	218.206 450	29.418 25	1.0403	45.38	26.10
SDSSJ151100.64+342842.4	227.752 670[a]	34.478 45[a]	1.4395	45.29	26.39
SDSSJ153044.08+231013.4	232.683 666	23.170 41	1.4068	46.09	25.88
SDSSJ155436.68+285942.5	238.652 850	28.995 14	1.1879	46.01	25.84
SDSSJ160245.92+453050.3	240.691 330	45.513 98	1.4074	45.58	25.93
SDSSJ163023.12+384700.7	247.596 378	38.783 52	1.5275	45.16	26.31
SDSSJ165724.82+204559.5	254.353 437	20.766 55	1.4679	45.48	26.20
Outlier					
SDSSJ084255.56+580425.6	130.731 537	58.073 79	1.3384	45.72	26.29

Notes. 1, 4: Identifier and redshift from the SDSS DR7 QSO catalogue (Schneider et al. 2010).
2, 3: Coordinates from *Gaia*, except for [a], for which coordinates come from SDSS.
5: Rest-frame 6 μm luminosity from *WISE* photometry, in log erg s^{-1}.
6: Rest-frame 1.4 GHz luminosity from FIRST photometry, in log W Hz^{-1}.

practice, such visual determination of morphology is only accurate for sources with enough fidelity in the FIRST images. Based on our experience with such visual inspection, we used a 1.4 GHz flux density cut of 3 mJy and a peak S/N > 15 as a rule of thumb. Sources with a flux offset greater than a factor of 2 between FIRST and the 20 cm NRAO VLA Sky Survey (NVSS) were also excluded; this criterion identifies systems in which large extended radio lobes are resolved out by the FIRST imaging (Klindt et al. 2019).

Our final pool of candidate targets was chosen from both colour-selected categories (rQSOs and cQSOs) in a small redshift interval ($1.0 < z < 1.55$), display compact FIRST radio morphologies, and lie in a small interval in radio luminosity ($25.5 < \log L_{1.4} < 26.5$ W Hz^{-1}). The redshift interval was chosen to minimize Malmquist biases. The radio luminosity interval spans the low end of FIRST-detected radio QSOs at our redshifts of interest, a regime where the various differences between red and normal QSOs are most pronounced. As we discuss in Section 3.4, the relative radio-to-MIR luminosities of our targets formally place them in the 'radio-loud' regime.

From this pool, we refined our targets to a final set of 20 rQSOs and 20 cQSOs that were matched in redshift and $L_{6\mu m}$ with a tolerance of 0.05 and 0.2 dex, respectively. The SDSS identifiers, redshifts, $L_{6\mu m}$, and other key properties of the targeted QSOs are listed in Table 1. For brevity, in the rest of the text and figures in this paper,

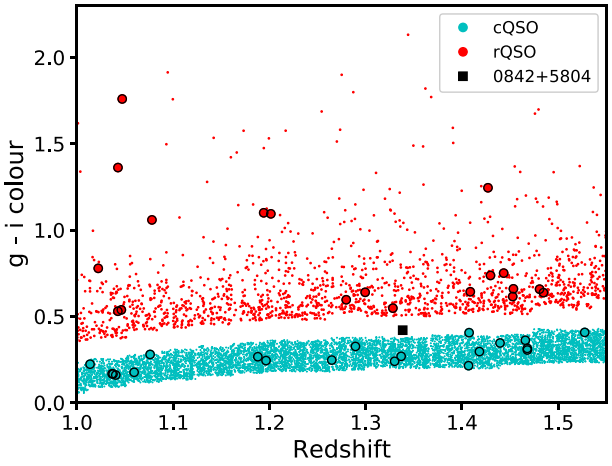

Figure 1. Observed frame Galactic extinction-corrected $g - i$ colours of SDSS DR7 QSOs in the redshift range of $1.0 < z < 1.55$ used in this study. The small coloured points are those of the parent sample after applying the colour selections for rQSOs (red points) and cQSOs (cyan points). More details may be found in Section 2.1.1. The targets for this e-MERLIN study are shown using larger points following the same colour scheme as above except for the single case of 0842+5804 (black square point), which was determined, after correction for Galactic extinction, to have a $g - i$ colour lying outside our colour-selection windows.

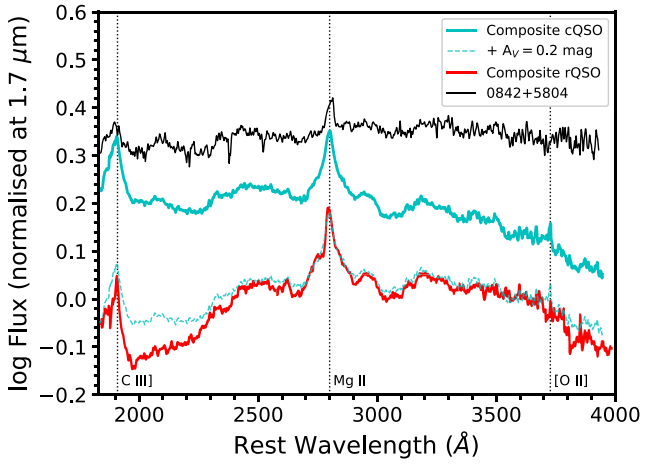

Figure 2. Composite rest-frame UV spectra of rQSOs (red solid) and cQSOs (cyan solid) derived from mean stacks of the SDSS spectra of our targets. The spectra were corrected for Galactic extinction and normalized to the rest-frame 1.7 μm fluxes of the corresponding QSOs before stacking. The cyan dashed line is a version of the cQSO composite that has been reddened by an SMC-like dust extinction law with $A_V = 0.2$ mag. The spectrum of 0842+5804 is separately shown in black, as it is an outlier in terms of colour and spectral properties.

we refer to the targets using a shortened form of the SDSS identifier: SDSSJ082314.71+560948.9 is shortened to 0823+5609, and so on.

2.1.2 *Sample properties*

In Fig. 1, we compare the $g - i$ colours against redshift of our e-MERLIN targets to those of SDSS DR7 QSOs from the parent sample of Klindt et al. (2019). Our targets are identified in the figure using larger symbols, and the plotting colour scheme of red/cyan for rQSOs/cQSOs that is used here will be reproduced consistently throughout the rest of the paper. In the post-observation analysis, we discovered that an incorrect level of Galactic extinction was originally applied to one of our targets (0842+5804), which initially selected it as an rQSO. With its updated Galactic extinction correction, its $g - i$ colour now places it closer to the cQSOs in Fig. 1. Hence, we do not consider it as an rQSO for the rest of our analysis. We discuss this object in more detail in Section 2.1.3.

All the rQSOs and 18 of the 20 cQSOs have estimates of black hole masses and Eddington ratios from the value-added catalogue of spectral properties of SDSS QSOs from Rakshit, Stalin & Kotilainen (2020). We find a range in masses (10^8–10^{10} $M_\odot$) and Eddington ratios (0.02–0.83) in our e-MERLIN targets, consistent with that of the parent sample at their redshifts. Since the nature of the radio source emission is broadly related to the Eddington ratios of AGN (Best & Heckman 2012), we note that our rQSOs and cQSOs have similar median Eddington ratios of 0.12 and 0.15, respectively. These high values confirm that rQSOs and cQSOs both harbour AGN powered by emission from a radiatively efficient accretion disc. Therefore, differences in their nuclear engines are unlikely to be the root cause of any differences in their radio properties.

The bright nuclei of our optically luminous QSO targets prevent a characterization of their host galaxies. Assuming these are representative of the hosts of typical $z \sim 1$ radio-loud QSOs, we expect them to be mostly bulge-dominated massive galaxies (e.g. Kukula et al. 2001), with moderate-to-strong levels of star formation ($\sim$100 $M_\odot$ yr^{-1}; e.g. Podigachoski et al. 2015). This is consistent with the extrapolation of trends found at low redshifts, where radiatively efficient 'high-excitation' radio AGNs are hosted by galaxies with substantial bulges, and discs that feature ongoing star formation (e.g. Smolčić 2009; Best & Heckman 2012). However, there is no clear evidence that rQSOs have different host properties from cQSOs at $z \sim 1$ (Calistro Rivera et al. 2021), and the contaminating effects of host galaxy light are not responsible for the red colours of rQSOs (see Klindt et al. 2019, and discussion below).

Fig. 2 compares the composite rest-frame UV spectra of the 20 cQSOs and 19 rQSOs. These composites are derived by taking a mean of the stack of their SDSS spectra, after correction for Galactic extinction by a Milky Way law of Fitzpatrick (1999). Before stacking, the spectra were normalized to the flux of the QSOs at a rest-frame wavelength of 1.7 μm, determined from a linear interpolation of their *WISE W1* and *W2* fluxes. As the rest-frame near-infrared luminosities of rQSOs are minimally affected by the small intrinsic dust columns that redden these systems, with this choice of spectral normalization, we are able to demonstrate the combined effects of dust extinction as well as reddening.

As mentioned earlier, the ensembles of rQSOs and cQSOs have approximately equal MIR luminosities since they are matched in $L_{6\mu m}$. Therefore, most of the differences in the overall flux of their median rest-frame UV spectra are attributable to the differences in intrinsic dust extinction and reddening among the rQSOs. We demonstrate this using the dashed cyan line in Fig. 2, which arises from the application of a simple dust screen model to the cQSO composite adopting an SMC-like extinction law (Pei 1992) set to $A_V = 0.2$ mag. Both the normalization and much of the shape of the rQSO composite are compatible with the effects of mild columns of intervening dust.

We note differences in some of the spectral features in these composites, such as trough around the C III] λ1909 line and the equivalent width of the narrow [O II] λ3727 line. We refrain from a discussion of these differences in this work; a detailed statistical

treatment of spectral differences between red and blue QSOs is the topic of a future paper from our team.

2.1.3 0842+5804: an outlier

0842+5804 was initially selected as an rQSO, but subsequent reanalysis of its Galactic foreground extinction placed its intrinsic colour closer to those of the cQSOs. Its estimated Galactic visual extinction of $A_V = 0.275$ is 0.23 mag higher than the median extinction suffered by our targets, and 0.08 mags higher than the next most extinguished QSO. It lies in the vicinity of a high-Galactic latitude dust filament. It is possible that its estimate of extinction, derived from the average of a 5 arcmin region surrounding the QSO, could be incorrect.

The spectrum of 0842+5804 is plotted in Fig. 2 with a black line to contrast it with the mean composite spectra of the cQSOs and rQSOs. Its normalization is higher than both the composites because it has the bluest MIR-to-optical colour of our entire sample. Despite this, it shows a UV spectral shape that is a bit redder than the median cQSOs. It also shows the weakest Mg II λ2800 equivalent width among our targets, as well as weaker than average Fe II band emission. 0842+5804 is an outlier in both its reddening and its spectral features.

In light of these complexities, we will exclude 0842+5804 from the statistical comparison of rQSOs and cQSOs, which is the main theme of this work. The exclusion of this one source does not greatly compromise the matched $L_{6\mu m}$ distributions that were the basis for the initial sample selection. For completeness, we will continue to include it in the figures of this section, but we distinguish it using a black plotting colour. It serves as a useful test of the methods we employ to identify extended structure from our eMERLIN data.

2.2 Astrometrically accurate QSO positions

The high angular resolution and milliarcsecond astrometric accuracy of the e-MERLIN data surpass the astrometric capabilities of the SDSS, which could make a comparison of the optical and radio positions of the QSOs difficult. We overcame this limitation by searching the *Gaia* DR2 catalogue (Gaia Collaboration 2018) for counterparts to our targets. Due to their optical brightness and point-like nature, 39 QSOs have a *Gaia* measurement, providing submilliarcsecond positional accuracies. In the various figures of this paper where the optical positions of the targets are shown, e.g. Fig. 3, we use these *Gaia* positions except for the cQSO 1511+3428, for which only the SDSS position is available.

2.3 TGSS 150 MHz fluxes

The TIFR GMRT Sky Survey (TGSS) is a 150 MHz imaging survey of 90 per cent of the sky using the Giant Metrewave Radio Telescope (GMRT), reaching a median noise level of 3.5 mJy. As part of TGSS Alternative Data Release (ADR; Intema et al. 2017), a catalogue of sources with a detection threshold of 7σ was published. As our targets are compact in FIRST, we assume that the TGSS source photometry, obtained from images with a beamsize of ≈30 arcsec, captures all of their 150 MHz flux, though blending with nearby sources may be a source of potential contamination.

39 of our e-MERLIN targets are covered by TGSS; one target, 0828+2731, lies at the edge of a hole in the survey coverage. 8 are associated with single TGSS detections within 5 arcsec, which we take to be their TGSS counterparts. We use these TGSS fluxes, in addition to default limits for the non-detections, in our analyses of radio spectral indices in Section 3.3.

2.4 1.4 GHz e-MERLIN imaging

2.4.1 Observations and reduction

Our 40 targets were observed with the e-MERLIN interferometer using its *L*-band receivers (1.23–1.74 GHz). Details of the observations are given in Table 2. Six antennas were used for all the observations; the large Lovell telescope was not used due to refurbishment work at the time, but the sensitivity of the reduced array was adequate for the science goals of this work. The 512 MHz bandwidth covered by the continuum correlator was split into 8 spectral windows of 128 channels each. Shortest integration intervals of 3–4 s were used.

The observations were carried out over seven separate runs: six in 2018 December and an additional short run in 2019 March to reobserve a target with better calibration. Each run consisted of a sequence of calibration scans interspersed with science scans on targets. To maximize *uv* coverage, the ≈1 h on-source time on each target was split into several sets of typically three short scans (a few minutes each) separated by 1–2 h. 3C 286 (1331+3030) was used as a flux reference for all runs.

OQ208 (1407+2827) was used as the primary bandpass calibrator and 3C 84 (0319+4130) was used as a pointing calibrator for most of the runs. During runs `CY7220_L_002_20181214` and `CY7220_L_004_20181218`, strong winds led to the premature parking of one of the antennae in the array before it could observe the nominal bandpass calibrator. Therefore, OQ208 was only used as a pointing calibrator in `CY7220_L_004_20181218`, and 3C 84 served as the primary bandpass reference. Complex gain calibrators observed throughout the run were bootstrapped for bandpass corrections to recover the data from the associated baselines from the troublesome antenna. In the case of `CY7220_L_002_20181214`, 3C 84 was used to calibrate the bandpass of the antenna after it was brought back to operation.

The radio data were reduced using the newly developed e-MERLIN pipeline, which employs a backbone of functions from the Common Astronomy Software Applications (CASA) package to flexibly average, flag, calibrate, and image data from the e-MERLIN correlator. For a few targets with faint phase calibrators, and for the entire `CY7220_L_005_20181220` run taken under windy conditions, we adapted the parameters from the pipeline (in particular the averaging intervals for calibration solutions and associated minimum flagging thresholds) to ensure that most of the data were unflagged and calibration solutions were suitable.

Since the same bandpass and pointing calibrators were used in all seven runs, we examined their calibrated flux densities to determine the relative flux calibration of our observations. The largest variations were found for the pointing calibrator that was often observed at a different part of a run sequence than the flux and bandpass calibrators. We measured the maximal range of the flux scale of the pointing calibrator to be ≈9 per cent, and we conservatively adopt this as the relative flux calibration uncertainty of our observations.

Using CASA, we post-processed the pipeline products for the science targets. In some cases, a small amount of manual flagging was needed to deal with residual RFI and phase errors. We also performed self-calibration on our targets to reduce residual phase and amplitude noise and deal with cases where a nearby bright source was affecting the images of the target.

Using WSCLEAN v2.6, we produced final images of our targets with a spatial sampling of 0.03 arcsec per pixel and a size of 15.36 arcsec

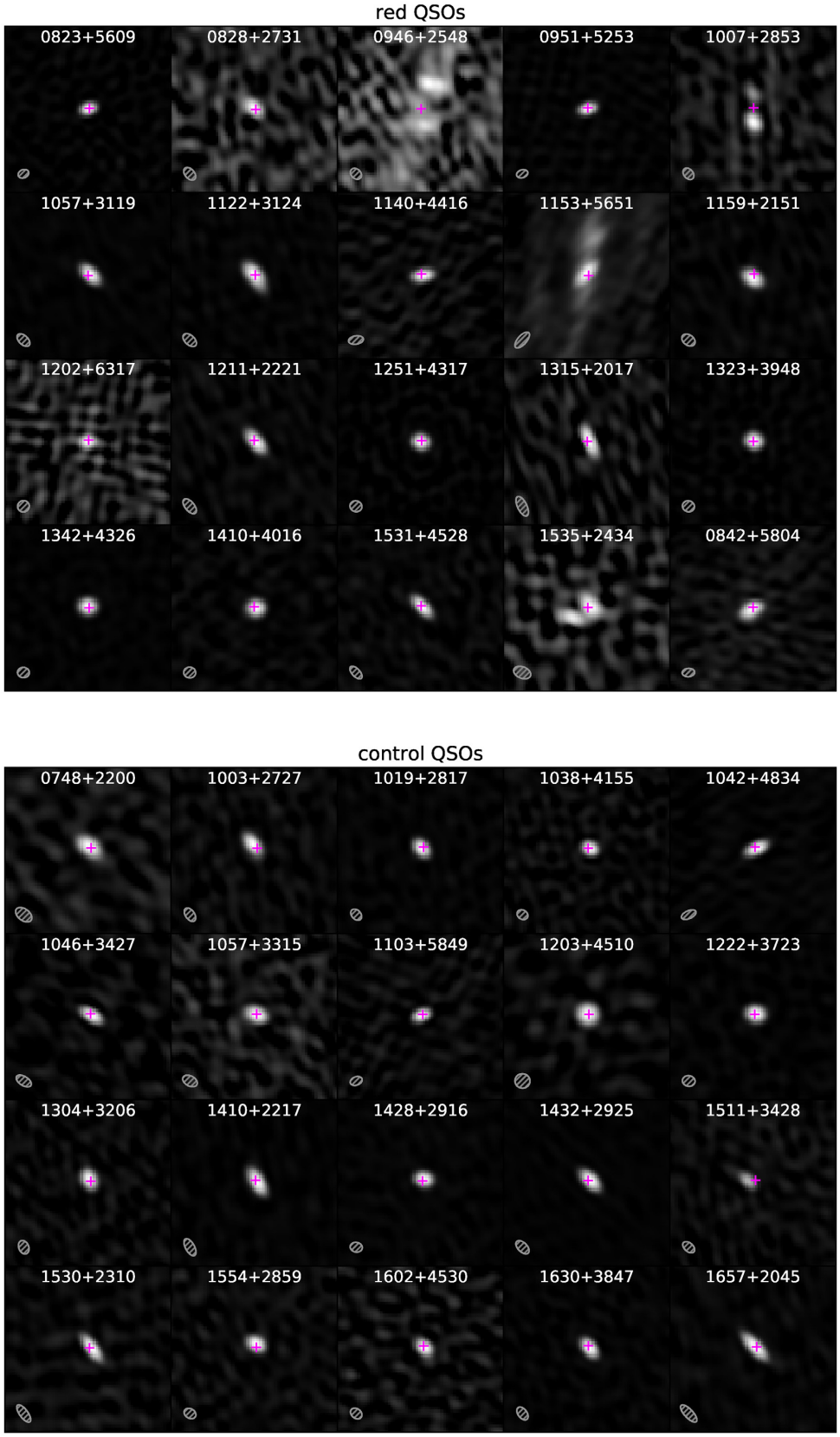

Figure 3. 2 arcsec × 2 arcsec stamps from our e-MERLIN images centred on the *Gaia*-based position of the targeted QSOs (magenta crosses). The top panels show the rQSO targets, including the outlier case of 0842+5804 that was initially selected as an rQSO (Section 2.1.3). The bottom panels show the cQSO targets. In each panel, a small hatched grey ellipse shows the size and shape of the restoring beam.

Table 2. Details of the e-MERLIN observations.

SDSS identifier (1)	Run ID (2)	RMS (3)	Peak (4)	Extended? (5)
Red QSOs				
SDSSJ082314.71+560948.9	CY7220_L_004_20181218	0.07	10.55	No
SDSSJ082837.75+273136.9	CY7220_L_002_20181214	0.06	1.19	No
SDSSJ094615.01+254842.0	CY7220_L_002_20181214	0.08	1.06	Yes
SDSSJ095114.35+525316.7	CY7220_L_004_20181218	0.08	10.71	No
SDSSJ100713.68+285348.4	CY7220_L_002_20181214	0.08	4.23	Yes
SDSSJ105705.15+311907.8	CY7220_L_001_20181214	0.06	13.38	No
SDSSJ112220.45+312440.9	CY7220_L_001_20181214	0.06	9.16	Yes
SDSSJ114046.80+441609.8	CY7220_L_004_20181218	0.09	5.63	No
SDSSJ115313.06+565126.3	CY7220_L_004_20181218	0.09	6.01	Yes
SDSSJ115924.05+215103.0	CY7220_L_001_20181214	0.08	9.31	No
SDSSJ120201.91+631759.4	CY7220_L_006_20181220	0.10	2.26	No
SDSSJ121101.81+222106.7	CY7220_L_001_20181214	0.06	4.82	No
SDSSJ125146.34+431729.7	CY7220_L_006_20181220	0.09	34.58	No
SDSSJ131556.37+201701.6	CY7220_L_003_20181216	0.10	3.82	No
SDSSJ132304.23+394855.0	CY7220_L_006_20181220	0.06	10.84	No
SDSSJ134236.96+432632.1	CY7220_L_006_20181220	0.06	20.14	No
SDSSJ141053.19+401618.5	CY7220_L_006_20181220	0.06	6.03	No
SDSSJ153133.53+452841.6	CY7220_L_005_20181220	0.07	6.26	No
SDSSJ153555.27+243428.6	CY7220_L_005_20181220	0.14	4.78	Yes
Control QSOs				
SDSSJ074815.44+220059.4	CY7220_L_002_20181214	0.11	4.46	No
SDSSJ100318.93+272734.3	CY7220_L_002_20181214	0.08	6.31	No
SDSSJ101935.22+281738.9	CY7220_L_002_20181214	0.08	11.05	No
SDSSJ103850.89+415512.7	CY7220_L_002_20181214	0.08	5.66	No
SDSSJ104240.11+483403.4	CY7220_L_004_20181218	0.09	12.20	No
SDSSJ104620.18+342708.4	CY7220_L_001_20181214	0.28	28.04	No
SDSSJ105736.17+331545.9	CY7220_L_001_20181214	0.06	2.10	No
SDSSJ110352.48+584923.5	CY7220_L_004_20181218	0.12	9.15	No
SDSSJ120335.39+451049.5	CY7220_L_006_20181220	0.54	42.27	No
SDSSJ122221.37+372335.8	CY7220_L_006_20181220	0.06	10.82	No
SDSSJ130433.42+320635.5	CY7220_L_001_20181214	0.09	6.81	No
SDSSJ141027.58+221702.6	CY7220_L_003_20181216	0.09	15.68	Yes
SDSSJ142824.76+291606.7	CY7220_L_007_20190327	0.08	13.26	No
SDSSJ143249.54+292505.7	CY7220_L_003_20181216	0.05	17.76	No
SDSSJ151100.64+342842.4	CY7220_L_003_20181216	0.06	4.28	Yes
SDSSJ153044.08+231013.4	CY7220_L_005_20181220	0.14	8.73	No
SDSSJ155436.68+285942.5	CY7220_L_003_20181216	0.09	5.39	No
SDSSJ160245.92+453050.3	CY7220_L_005_20181220	0.15	7.27	No
SDSSJ163023.12+384700.7	CY7220_L_005_20181220	0.07	9.90	No
SDSSJ165724.82+204559.5	CY7220_L_005_20181220	0.09	9.36	No
Outlier				
SDSSJ084255.56+580425.6	CY7220_L_004_20181218	0.10	6.64	Yes

Notes. 1: Identifier from the SDSS DR7 QSO catalogue (Schneider et al. 2010).
2: e-MERLIN identifier for the observing run.
3: Root mean square (RMS) flux density of the final cleaned image (3σ clipped; mJy per beam).
4: Peak flux density of the final cleaned image (mJy per beam).
5: As determined from both visual assessment and core/beam analysis of the eMERLIN images.

(512 × 512 pixels). The image size was chosen to fully cover the 5 arcsec-resolution element of the FIRST survey with enough margin to pick up any structure that may have been barely resolved in FIRST. The choice of pixel size ensured that the images sampled across the minor axis of the highest resolution data set with at least 3 pixels.

In Fig. 3, we show the inner 2 arcsec × 2 arcsec region of the final e-MERLIN images of all the QSOs from our sample. With the long baselines of e-MERLIN, the restoring beams of our images have a median major full width at half-maximum (FWHM) of 0.″18, which translates to projected scales of 1.48–1.56 kpc over the range of redshifts of our targets. Therefore, we resolve radio structures within the confines of the host galaxies of these QSOs, in contrast to the supergalactic scales (>40 kpc) that are probed by the 5 arcsec beam of their FIRST images.

2.4.2 *Gaussian image decomposition*

In order to characterize the radio source structure in the e-MERLIN images, we decomposed the images into a set of two-dimensional elliptical Gaussian components. For this, we used the ASTROPY MODELING subpackage, with minimization through its implementation

of a least-squares Simplex algorithm. We set fitting bounds on the Gaussian components to ensure positive amplitudes and sizes greater than 50 per cent of the corresponding restoring beam.[1]

In a first pass, we undertook a run of fits over the central 2 arcsec of each image adopting only a single Gaussian model that was initialized to match the shape of the restoring beam. After examining the fitting residuals visually, we flagged the five cases in which a single Gaussian did not adequately represent the source structure. Two more objects showed emission beyond the central 2 arcsec, which we also flagged. These seven images were then subjected to a second round of fits using multiple (>2) Gaussian components.

In each of the multiple-component fits, we first manually determined the number of components to apply to the fit, and estimated initial amplitudes, positions, and sizes for each component. After the fits, we examined the residuals and added or removed components as needed to capture most of the visual source structure. We required between two and four components to fit all the sources with initial evidence for extended structure. Since the noise in the e-MERLIN images has a large correlated component, we resorted to a visual judgement of the fit quality rather than taking a more quantitative metric. This lack of precision is not a major source of uncertainty for this work.

The results of the Gaussian decomposition of the e-MERLIN images are tabulated in Table 3, and a visualization of the final fits for all the targets is available in the online material (Supplementary Figs 1 and 2). In Section 3.1, we provide a detailed description of the extended radio structure among our targets.

2.4.3 Searching for additional extended sources

To complement the visual analysis described earlier, we developed an approach to search for additional extended source structure at the resolution limit of our images. This was performed only on the 33 sources for which a single-component fit was determined to be an adequate representation of the images. We distinguish between rQSOs and cQSOs in the analysis below, and also separately include the outlier QSO 0842+5804 because it serves as a useful validation of our technique.

We searched for evidence of extended structure through a comparison of the parameters of the single-component Gaussian fits with those of the restoring beam of the images. In the following description, we refer to this single component as the 'radio core'.

In the left-hand panel of Fig. 4, we plot the ratios of the semimajor axis of the radio core component to that of the beam, splitting rQSOs and cQSOs into different histograms. The distributions for most QSOs are centred about unity, indicating that these single-component systems are unresolved in our e-MERLIN imaging. 0842+5804, shown in black in Fig. 4, is the only visually compact object that has a significantly larger core size than the corresponding restoring beam. While its radio core is fitted well by a single Gaussian, the size of this component is ≈30 per cent larger than the beam, showing that it is definitely extended.

There is a mild suggestion that the ensemble of visually compact rQSOs is marginally larger than their beams, by 1.1 ± 0.25 per cent, in contrast to the ensemble of cQSOs that are consistent with unity at the same level of uncertainty. However, the distributions of core/beam size ratios for the two subsets are statistically indistinguishable with our current sample sizes.

[1]Fits to the images with the CASA IMFIT task gave us very similar results. In this work, we only report our ASTROPY-based modelling, as this approach allowed for greater flexibility in the choice of a robust minimization algorithm.

We also compare the best-fitting position angles (PAs) of the core components to those of their respective restoring beams (right-hand panel of Fig. 4). Most of the systems have core and beam PAs that agree within $\pm 10^{\circ}$. One rQSO (1202+6317) and one cQSO (1203+4510) have almost circular beams, and their core PAs are extremely uncertain, leading to large PA differences that are not significant. The only object with a definite difference between the core and beam PA is 0842+5804. Therefore, the relative core/beam size and PA analyses yield consistent results, identifying 0842+5804 as a QSO with extended emission that is not obvious from a visual assessment.

Taking advantage of the high astrometric accuracy of the e-MERLIN images and the QSO positions from *Gaia*, we search for angular offsets between radio core components and the optical positions of the unresolved or single-component sources. As the optical position is centred on the true AGN nucleus, a systematic measurable difference between the relative optical and radio centroid could indicate that the radio core contains asymmetric emission below the resolution of the e-MERLIN images, betraying the presence of radio structure on sub-kpc scales.

We first verified that the optical positional offsets of the radio core components distributed about a zero mean in both RA and Declination. This ensures that any systematic astrometric error between the e-MERLIN and *Gaia* reference frames is negligible, as expected. Translating the optical offsets to an angular distance in milliarcseconds (mas), we compare, in Fig. 5, the distributions of the offsets for our sample, split into colour-selected subsets.

We find that the single-component cQSOs and rQSOs show a similar range of offsets between their optical and radio core positions. Most lie within 30 mas, the size of a single pixel in our images and ≈1/6 of the typical beamwidth of the images. This scatter is consistent with the errors of the radio core centroids from our Gaussian component fits. There is a mild difference in the shape of the offset distributions between cQSOs and rQSOs, but we do not consider this to be significant based on a two-sided Kolmogorov–Smirnov (K–S) test.

Two objects show offsets in the long tail of the distribution: 0842+5804 and the cQSO 1003+2727. The evidence for extended structure in 0842+5804 has been presented earlier, and this may explain its larger offset. 1003+2727, on the other hand, has an image that is completely consistent with the restoring beam, yet the respective panel in Fig. 3 clearly shows a visible offset between the centre of its apparently unresolved core and the optical position. However, the gain calibration for this particular source was complicated by heavy flagging of the calibrator scans by the pipeline, and the final astrometric solution may be unreliable. In light of this, we do not place much weight on the apparent offset, and henceforth treat 1003+2727 as a single-component core-dominated source. Possible higher frequency e-MERLIN observations in the future may help us to verify its nature.

3 RESULTS

3.1 Visually extended radio sources

Five of our targets exhibit visually extended emission, both from an examination of the central images (Fig. 3) and based on their single-component Gaussian fits: 0946+2548, 1007+2853, 1122+3124, 1153+5651, and 1535+2434. All five are rQSOs. In two cQSOs that have unresolved cores, additional extended emission is seen on scales larger than the cut-outs: 1511+3428 shows a bright radio hotspot 5 arcsec away from its core, and 1410+2217 has a faint lobe-like structure 2.2 arcsec from the core.

Table 3. Results of Gaussian decomposition of the e-MERLIN images.

SDSS identifier (1)	RA (2)	Declination (3)	Flux density (4)	Major axis (5)	Axial ratio (6)	PA (7)
			Single-component fits			
SDSSJ074815.44+220059.4	117.064 356	22.016 52	4.6	0.23	1.65	49.6
SDSSJ082314.71+560948.9	125.811 277	56.163 61	11.0	0.13	1.35	110.0
SDSSJ082837.75+273136.9	127.157 346	27.526 91	1.4	0.19	1.61	50.3
SDSSJ084255.56+580425.6	130.731 569	58.073 78	11.1	0.20	1.58	120.5
SDSSJ095114.35+525316.7	147.809 856	52.887 96	11.7	0.15	1.51	107.8
SDSSJ100318.93+272734.3	150.828 926	27.459 56	7.0	0.20	1.73	34.3
SDSSJ101935.22+281738.9	154.896 744	28.294 16	11.8	0.15	1.38	38.1
SDSSJ103850.89+415512.7	159.712 043	41.920 18	5.7	0.13	1.22	67.5
SDSSJ104240.11+483403.4	160.667 154	48.567 62	13.2	0.19	1.93	115.1
SDSSJ104620.18+342708.4	161.584 125	34.452 33	25.1	0.19	1.92	58.6
SDSSJ105705.15+311907.8	164.271 490	31.318 82	14.1	0.19	1.69	45.6
SDSSJ105736.17+331545.9	164.400 738	33.262 75	2.2	0.18	1.44	69.3
SDSSJ110352.48+584923.5	165.968 715	58.823 18	8.8	0.14	1.47	113.6
SDSSJ114046.80+441609.8	175.195 025	44.269 38	5.5	0.18	1.73	100.6
SDSSJ115924.05+215103.0	179.850 226	21.850 82	9.4	0.18	1.40	53.5
SDSSJ120201.91+631759.4	180.508 065	63.299 83	2.1	0.15	1.29	88.7
SDSSJ120335.39+451049.5	180.897 500	45.180 43	40.9	0.17	1.03	105.6
SDSSJ121101.81+222106.7	182.757 572	22.351 87	5.0	0.22	1.92	38.9
SDSSJ122221.37+372335.8	185.589 098	37.393 29	12.0	0.16	1.20	78.3
SDSSJ125146.34+431729.7	192.943 078	43.291 57	33.5	0.14	1.11	72.2
SDSSJ130433.42+320635.5	196.139 294	32.109 89	6.8	0.16	1.37	22.4
SDSSJ131556.37+201701.6	198.984 948	20.283 77	3.7	0.27	2.64	22.0
SDSSJ132304.23+394855.0	200.767 657	39.815 28	11.2	0.14	1.11	68.7
SDSSJ134236.96+432632.1	205.654 007	43.442 23	21.5	0.14	1.11	85.0
SDSSJ141053.19+401618.5	212.721 700	40.271 82	6.3	0.15	1.10	91.5
SDSSJ142824.76+291606.7	217.103 210	29.268 55	13.6	0.15	1.25	79.0
SDSSJ143249.54+292505.7	218.206 458	29.418 25	18.7	0.20	1.77	44.1
SDSSJ153044.08+231013.4	232.683 674	23.170 39	8.5	0.24	2.48	35.8
SDSSJ153133.53+452841.6	232.889 736	45.478 21	7.2	0.20	2.02	43.1
SDSSJ155436.68+285942.5	238.652 863	28.995 14	6.0	0.15	1.30	58.3
SDSSJ160245.92+453050.3	240.691 333	45.513 97	7.4	0.16	1.42	45.0
SDSSJ163023.12+384700.7	247.596 391	38.783 51	10.3	0.17	1.61	38.0
SDSSJ165724.82+204559.5	254.353 443	20.766 54	9.7	0.26	2.50	43.0
			Multiple-component fits			
SDSSJ094615.01+254842.0	146.562 520	25.811 63	0.6	0.16	1.31	65.9
	146.562 515	25.811 77	0.9	0.15	1.49	65.2
	146.562 468	25.811 76	0.5	0.10	0.85	− 89.9
	146.562 552	25.811 66	13.7	2.13	5.92	− 19.8
SDSSJ100713.68+285348.4	151.806 988	28.896 73	4.9	0.17	1.41	21.8
	151.806 990	28.896 82	1.7	0.17	1.44	18.2
SDSSJ112220.45+312440.9	170.585 230	31.411 38	10.2	0.21	1.80	41.2
	170.585 219	31.411 35	2.0	0.28	2.60	44.7
SDSSJ115313.06+565126.3	178.304 467	56.857 28	5.1	0.22	1.92	144.8
	178.304 431	56.857 40	1.3	0.23	2.02	120.3
	178.304 464	56.857 29	22.3	1.90	5.17	− 11.8
SDSSJ141027.58+221702.6	212.614 961	22.284 05	16.5	0.23	2.03	29.1
	212.615 037	22.283 44	3.1	0.42	2.00	− 75.5
	212.615 104	22.283 71	0.3	0.11	0.79	− 89.9
SDSSJ151100.64+342842.4	227.752 709	34.478 44	2.0	0.17	1.60	44.2
	227.754 067	34.479 28	7.8	0.21	1.28	44.9
SDSSJ153555.27+243428.6	233.980 320	24.574 60	5.9	0.23	1.50	36.4
	233.980 388	24.574 57	4.0	0.25	2.06	73.1

*Notes.*1: Identifier from the SDSS DR7 QSO catalogue (Schneider et al. 2010).
2, 3: Peak position of the component on the e-MERLIN image (degrees).
4: Observed e-MERLIN *L*-band flux density of the component (mJy).
5: Major axis FWHM of the component (arcsec).
6: Major-to-minor axial ratio of the component.
7: Position angle of the component, measured from North (°).

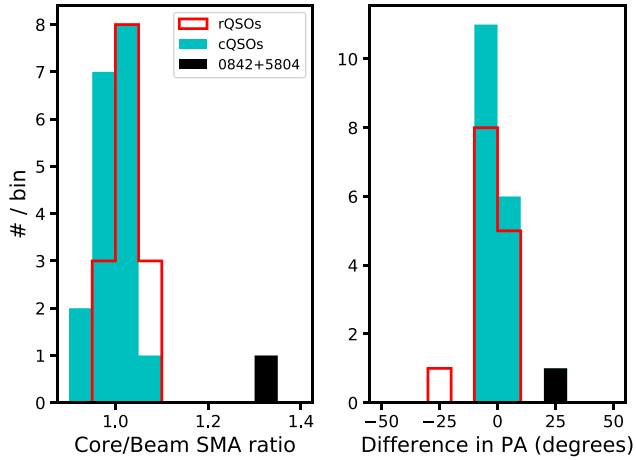

Figure 4. Left: The ratio of the semimajor axis of the core component to that of the restoring beam for sources that were visually determined to be compact in the e-MERLIN images. Most of the core components have sizes comparable to that of the beam, except for 0842+5804 (plotted in black). The distribution of core extensions of rQSOs is marginally larger than those of the cQSOs. Right: The difference in position angle between the core components and the restoring beam for sources that were visually determined to be compact in the e-MERLIN images. Except for 0842+5804 (plotted in black) and a few sources imaged with almost circular beams, the core components are aligned with their beams. From these two figures, we conclude that the majority of visually compact cores are unresolved in our e-MERLIN observations.

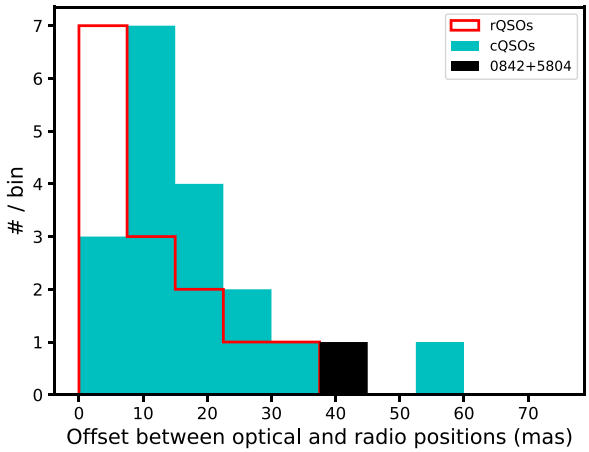

Figure 5. Spatial offsets between the *Gaia* positions of the optical QSOs and the fitted centres of the radio core components for the targets that were visually determined to be compact in the e-MERLIN images.

Here, we summarize the properties of these seven rQSOs and cQSOs with clearly extended emission. High-contrast images covering their full extent are shown in Figs 6 and 7, the multicomponent fits are shown in Supplementary Fig. 2 of the online material, and their parameters are summarized in the lower part of Table 3.

3.1.1 0946+2548

The presence of a nearby bright radio source affected the imaging of this object, leading to a high level of noise. The final self-calibration was performed on this nearby source, and then applied to the target.

The QSO radio source is composed of two bright resolved knots separated by 0.″5, along PA $= -17°$, which we take to define an axis for the system. The *Gaia* position of the QSO lies between the two main knots, coinciding with another faint knot that has a marginal S/N (Fig. 3).

The brighter north-western knot shows an extension perpendicular to the axis. There is a hint of diffuse patchy emission oriented along the axis that extends beyond the two knots, which may indicate partially recovered extended emission. We modelled the source using four components: two for the north-western knot, one for the south-eastern knot, and a large elongated component to capture the diffuse emission around the knots.

The elongated component dominates the total flux, but it may be influenced by residual *uv* noise in the image. This may explain the $\approx$2.5$\times$ greater flux that we measure in this source compared to its flux from the FIRST survey (Section 3.2).

3.1.2 1007+2853

The source consists of two compact components separated by 0.″34 along PA $= 0°$, which we modelled using two Gaussian components. The QSO position lies between the two components, suggesting that they are opposite lobes of a bipolar jet or outflow.

3.1.3 1122+3124

The source consists of a single dominant core component that shows a faint elongation along PA $= 205°$. A single-component fit leaves a definite visible residual along the direction of the elongation. Therefore, two components are required to fit the source adequately.

3.1.4 1153+5651

This source exhibits a complex morphology with a dominant central core and a bipolar extension along PA $= 171°$. In addition to the bright unresolved core, there is a mildly resolved knot 0.″42 away, from which a faint tendril of emission extends even further north. Towards the south, faint emission appears to outline the edge of a poorly defined lobe.

We model the source using three components, one each for the core, northern knot, and extended jet-like emission. The low S/N of the apparent lobe-like southern feature prevents it from being modelled.

3.1.5 1535+2434

The pipeline-calibrated images of this source were strongly affected by two bright sources a few arcminutes away. A first round of wide-field self-calibration was used to model the target as well as these bright nearby contaminants. After strong data averaging to smear out the effects of the other sources, a final round of self-calibration was performed on the target to obtain the final image.

The QSO radio source is composed of two bright knots separated by 0.″27 along PA $= 115°$. The *Gaia* position of the QSO is close to the centre of the western knot, which is also extended beyond the size of the beam.

3.1.6 1410+2217

This is one of two cQSOs with detectable extended emission. The source structure is dominated by a bright unresolved core. South of

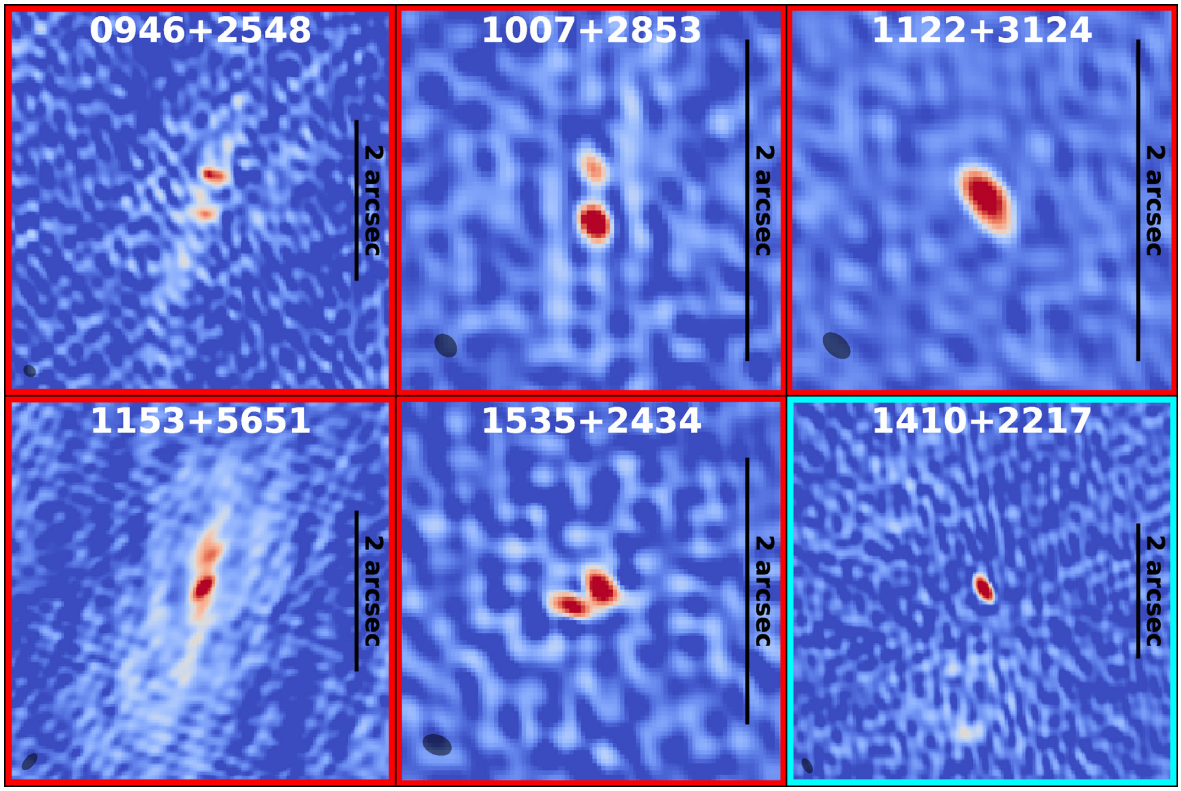

Figure 6. A montage of the visually extended sources from the e-MERLIN observations. A bar corresponding to a scale of 2 arcsec is shown to the right of each panel, which corresponds to the largest angular scale to which the observations are sensitive. Red or cyan coloured borders indicate whether the source is an rQSO or cQSO, respectively. Section 3.1 discusses these sources in more detail.

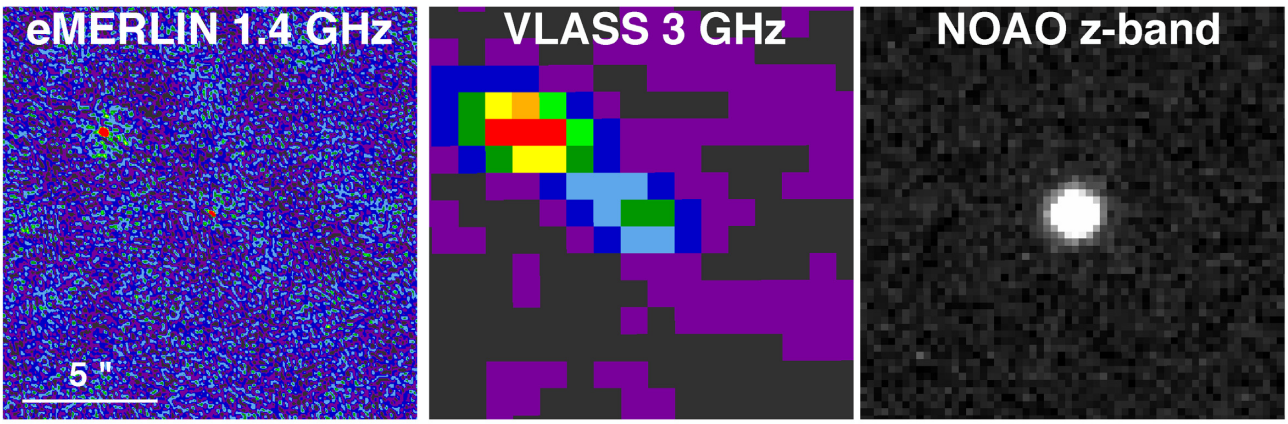

Figure 7. Images of the cQSO 1511+3428 from our e-MERLIN observations (left-hand panel), the VLA Sky Survey Quick Look (VLASS epoch1.1, middle panel), and the NOAO Legacy Surveys in the z band. The source is strongly one-sided; a bright knot is seen to the north-east of the core, but there is no detectable emission to the south-west. The z-band imaging does not show any optical source at the location of the north-east knot, so we cannot verify whether it corresponds to a galaxy in the vicinity of the QSO.

the core, 2.″25 away along PA = 173°, a faint arc-like feature marks the outer edge of a barely defined lobe. We modelled the source as a core component and two faint knots on the edge of this tentative lobe, which we manually adjusted and tied during the fit.

3.1.7 1511+3428

The QSO was selected for visual compactness in its FIRST imaging, but our e-MERLIN image clearly resolves it into two compact sources, of which the fainter source corresponds to the optical location of the QSO (Fig. 7). The two knots are separated by 5.″06 along PA = 53°. The core is unresolved, but the north-eastern knot has an FWHM that is 25 per cent larger than the restoring beam, indicating a moderately resolved structure.

The brighter north-eastern knot could be one hotspot of an asymmetric FRII-like radio galaxy. Neither FIRST or VLASS images, or a natural-weighted large-scale image of the e-MERLIN data, show any evidence of a south-eastern counterpart to the north-eastern knot. Therefore, if this is a bipolar radio galaxy, the two lobes would need to have a high contrast of greater than ≈70. The VLASS Quick Look

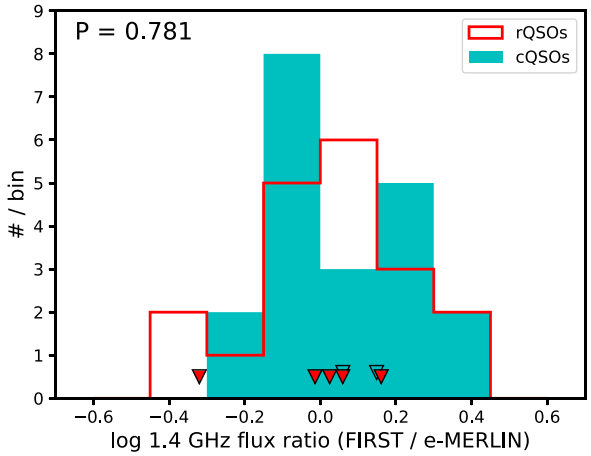

Figure 8. The ratio of the total measured e-MERLIN flux to the FIRST flux for the radio QSOs from our study; rQSOs (red open histogram) and cQSOs (cyan closed histogram) are plotted separately. The number in the upper left is the probability that the flux ratios of the cQSOs and rQSOs are drawn from the same parent distribution as determined by a K–S test. The downward triangles mark the flux ratios for the five rQSOs (red points) and two cQSOs (cyan points) that have extended radio emission in their e-MERLIN images. The cQSO points have been slightly offset vertically in the figure only to improve their visibility.

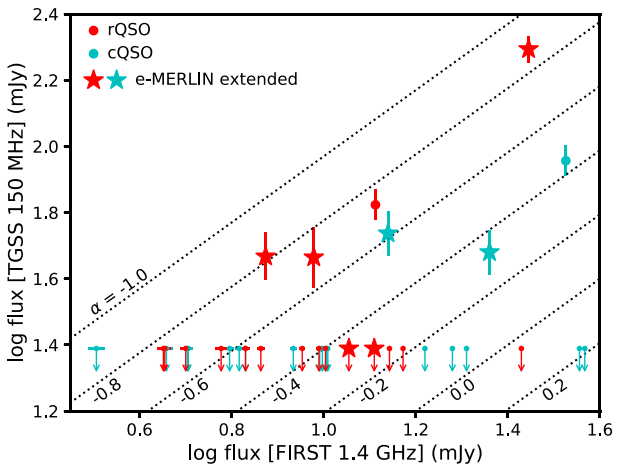

Figure 9. 1.4 GHz flux densities from FIRST plotted against 150 MHz flux densities from TGSS for the QSOs in our sample. The diagonal dotted lines mark tracks of constant radio spectral index between the two frequencies, ranging from an inverted spectrum ($\alpha = 0.2$) in the lower right to a steep spectrum ($\alpha = -1$) towards the middle left. QSOs that are extended in the e-MERLIN images are shown with larger star-shaped points. The upper limits are plotted at 24.5 mJy, the median detection limit of the TGSS survey.

image shown in Fig. 7 suggests a hint of emission between the core and knot, which lends credence to the radio galaxy interpretation.

Moderately deep optical imaging of the region around the QSO from the NOAO Legacy surveys does not show any optical counterpart at the location of the north-eastern knot, which also supports its hotspot nature. On the other hand, at the depth of the optical image ($z = 23$ AB mag), the corresponding limit on the equivalent rest-frame U-band luminosity of any galaxy at the redshift of the QSO ($z = 1.439$) yields a stellar mass of $\approx 7 \times 10^{10}$ $M_{\odot}$, taking a solar-metallicity simple stellar population with an age of $\approx$1.5 Gyr, a reasonable model for a radio-loud galaxy host in the environment of the QSO. The limit is only weakly dependent on the age or metallicity of the assumed stellar population. Clearly, a rather massive galaxy in the vicinity of the QSO could remain undetected with the available optical imaging, if it was quiescent or dusty. Therefore, the absence of a visible optical counterpart to the north-eastern knot should not be taken as strong evidence that this object is a large asymmetric radio galaxy centred on the QSO.

3.2 FIRST versus e-MERLIN radio fluxes

The e-MERLIN interferometer has an L-band maximum angular scale of $\approx$2 arcsec: Our images are not sensitive to radio structures that are larger than these scales. In contrast, the resolution of FIRST is at least 5 arcsec across. Therefore, our radio QSOs could potentially have extended radio emission that is invisible to e-MERLIN, yet remains unresolved with FIRST.

We can search for evidence of this by comparing the L-band radio fluxes from FIRST to the fluxes we have measured from the e-MERLIN images through our Gaussian component analysis (Section 2.4.2). A significant and systematic excess of FIRST fluxes over e-MERLIN fluxes would suggest radio emission that is resolved out by e-MERLIN.

In Fig. 8, we plot the FIRST-to-e-MERLIN flux ratio distributions of the rQSOs and cQSOs separately. The median ratio for rQSOs is 1.06, compared to 1.02 for cQSOs; the difference is not significant given the substantial scatter of the observed flux ratios (standard deviations of $\approx$0.2 dex). This is verified through a two-sided K–S test, which indicates that the two distributions have an 80 per cent chance of being drawn from a common parent sample.

The observed scatter of the flux ratios is larger than the estimated flux scale uncertainty of our observations ($<$10 per cent; Section 2.4.1). Therefore, we attribute these flux differences primarily to radio source variability in these compact QSOs over the $\approx$8 yr that separate the epochs of the FIRST and e-MERLIN observations. Since the flux ratios of the rQSOs and cQSOs do not differ significantly, we conclude that neither subsample shows any conclusive evidence for the widespread presence of bright radio structure extending beyond a few arcsec ($\gtrsim$15 kpc at the redshifts of our QSOs).

Having said this, the seven sources with visual extended structure (downward pointing triangular points in Fig. 8) have flux ratios that are generally shifted towards positive values, which may result from low-level extended emission from radio lobes that has been resolved out. This emission is unlikely to dominate the radio flux in these sources. The rQSO with a negative ratio is 0946+2548, where the e-MERLIN flux estimate comes primarily from the large low-surface brightness component that is poorly constrained, and possibly overestimated. While we can trust the accuracy of the e-MERLIN flux estimates for the core-dominated unresolved sources, the resolved sources could have larger errors. As the FIRST fluxes will be reliable for all our sources, we only use these in the following analyses of radio properties, keeping in mind that variability sets a systematic scatter of a factor of 2 on $L_{1.4}$.

3.3 Radio spectral indices

Fig. 9 plots the 1.4 GHz and 150 MHz flux densities of the 39 QSOs with coverage in the TGSS ADR (Section 2.3). The dotted diagonal lines delineate tracks of constant radio spectral index α, where the flux density at a radio frequency ν is given by $S_{\nu} \propto \nu^{\alpha}$.

The spectral indices of the eight TGSS-detected QSOs span values from -0.4 to -0.8, fairly typical for AGN-powered radio sources.

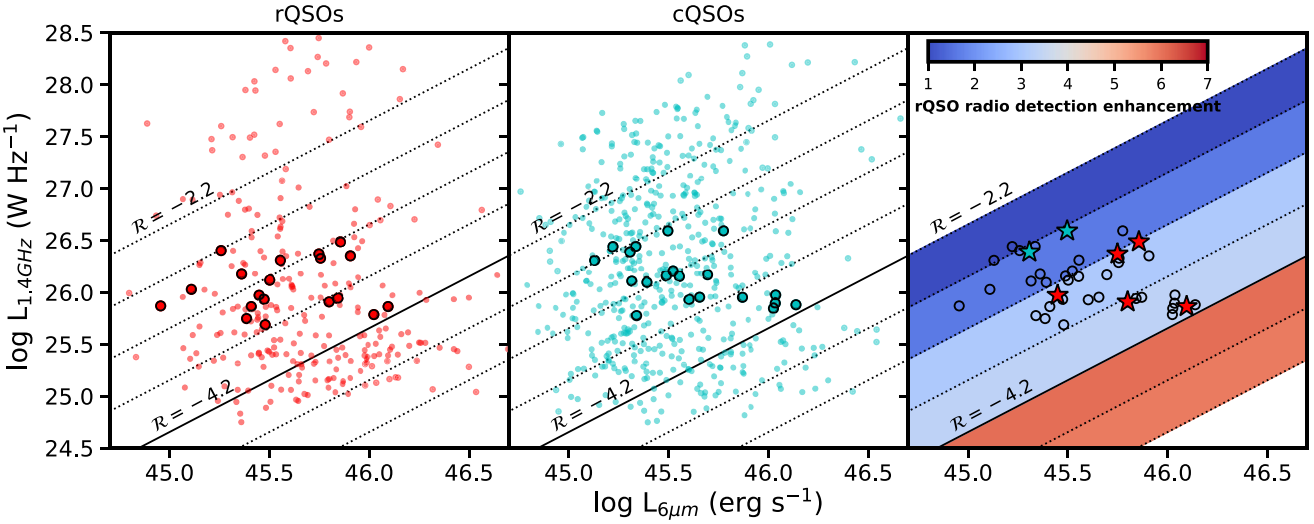

Figure 10. $L_{6\mu m}$ versus $L_{1.4}$ for rQSOs (left-hand panel) and cQSOs (middle panel) from the parent sample (small coloured points) in the redshift range of $1.0 < z < 1.55$ used in this study. The e-MERLIN targets are shown as large coloured points in the respective panels. Diagonal lines in all three panels show lines of constant 'radio-loudness' $\mathcal{R}$, as defined in Section 3.4. The solid diagonal line marks the approximate transition between 'radio-loud' and 'radio-quiet' sources. In the right-hand panel, we plot the relative enhancement in the radio detection rate of rQSOs versus cQSOs in the indicated bins of $\mathcal{R}$, as measured from the very same populations of QSOs plotted in the left-hand and middle panels. The detection rate enhancement increases towards low values of $\mathcal{R}$ (see also Klindt et al. 2019). The points plotted in the right-hand panel are the e-MERLIN targets of this study, and the sources with visually extended emission are distinguished as red star points (five rQSOs) and cyan star points (two cQSOs).

For the rest, we show typical 7σ (=24.5 mJy) upper limits on the 150 MHz flux densities. These span a large range of possible spectral indices, and some of the QSOs that are bright in FIRST are expected to have flat or inverted spectra, characteristic of very compact core-dominated radio sources. Conversely, the 150 MHz fluxes of the TGSS-detected sources could arise from very extended steep-spectrum lobes that do not appear in either FIRST or NVSS images. Future LOFAR public survey data will help discriminate between compact and extended low-frequency radio components.

Six of the TGSS detections also show extended emission in their e-MERLIN images, which is consistent with their nature as more evolved radio sources (Section 4.3.2). The two rQSOs with extended structure that remain undetected in TGSS (1122+3124 and 1535+2434) are also the most core dominated, and their limits suggest a typical flat-spectrum core.

3.4 The MIR–radio plane

In Fig. 10, we plot the MIR luminosity ($L_{6\mu m}$) against the FIRST-based rest-frame 1.4 GHz luminosity ($L_{1.4}$) of colour-selected QSOs from the parent sample in our working redshift interval. rQSOs and cQSOs are plotted in the left-hand and middle panels, respectively. As noted in our earlier works, there is no clear relationship between MIR and radio luminosities, with both spanning orders of magnitude within the parent sample (Klindt et al. 2019; Fawcett et al. 2020; Rosario et al. 2020). However, there is a clear difference between cQSOs and rQSOs in the distribution of radio luminosities in this plane. This is evident if we compare the fraction of cQSOs and rQSOs across the $L_{1.4}$–$L_{6\mu m}$ ratio, a quantity, when converted into $\log_{10}$ units, that we define as the 'radio-loudness' $\mathcal{R}$. We refer the reader to Klindt et al. (2019) and Rosario et al. (2020) for a detailed discussion of the $\mathcal{R}$ parameter in relation to traditional radio-loudness measures, but highlight here that the value of $\mathcal{R} = -4.2$ corresponds to the typical radio-loud/-quiet divide, such that more radio-loud systems have a higher value of $\mathcal{R}$.

In all three panels of Fig. 10, we plot diagonal lines that mark constant values of $\mathcal{R}$. The solid diagonal line corresponds to the characteristic threshold value of $\mathcal{R} = -4.2$. Earlier work from our team (Klindt et al. 2019; Rosario et al. 2020) has shown that radio-intermediate rQSOs have a significantly higher incidence within the QSO population; i.e. the enhancement in the radio detection rate of rQSOs over that of cQSOs is highest for systems that have an $\mathcal{R}$ value around the solid line in Fig. 10. We can demonstrate this visually by splitting the rQSOs and cQSOs in the left-hand and middle panels into bins of $\mathcal{R}$ and plotting their relative numbers, normalized by the size of the respective parent subsamples to account for the larger number of cQSOs drawn from the parent sample. This is shown in the right-hand panel of Fig. 10. Among the most radio-loud QSOs, towards the top left of the panel, the relative incidences of rQSOs and cQSOs are similar, but moving towards the bottom right and decreasing in $\mathcal{R}$, rQSOs become significantly more numerous with respect to cQSOs until the radio detection limit of FIRST cuts in. Around the radio-loud/quiet boundary, there are ≈5 times more rQSOs detected in the radio than cQSOs if one considers equally populated subsets of the parent sample.

We can now examine the trends shown by our e-MERLIN targets on the MIR-radio plane within the context of the coeval parent QSO population. The targets are shown as large circular points in their respective panels in Fig. 10. The narrow range in radio luminosity used to select our targets ($25.5 < \log L_{1.4} < 26.5$ W Hz^{-1}) is evident, as well as the fact that they are matched in $L_{6\mu m}$.

The targets are all plotted together in the right-hand panel of Fig. 10, where we have additionally highlighted those sources with extended emission as large coloured star points. Interestingly, the sources seem to cluster differently on this plane depending on their classification. The two extended cQSOs lie to the upper left of the range shown by our targets, in the domain of $\mathcal{R}$ that marks them as being quite radio loud. On the other hand, the five rQSOs with extended emission lie to the right and bottom right,

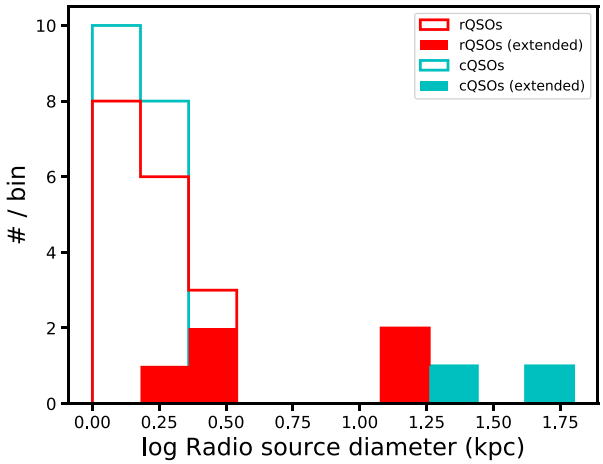

Figure 11. Maximum projected radio source diameters of the QSOs in our sample, measured from Gaussian fits to the e-MERLIN images and converted to physical units. Resolved sources are shown using filled histograms and the limits on the core sizes of the unresolved sources are shown using open histograms.

increasingly close to the radio-intermediate regime where rQSOs are most overrepresented in the overall QSO population.

3.5 Physical sizes

Even a cursory examination of Fig. 6 reveals qualitative differences in the appearance of the visually extended rQSOs and cQSOs. All five rQSOs show complex, knotty structure, often on small scales, while the two cQSOs display single unresolved cores and larger hotspots or lobes. This can be quantitatively assessed through a comparison of the physical sizes of the rQSOs and cQSOs.

We define the maximum size of our sources as either the largest separation between any two Gaussian subcomponents or the major-axis width of the largest single component, whichever is larger. In the case of sources that only have a single core component, its major-axis width is adopted as a limit on the source size. We transcribe the measured angular sizes to physical sizes using the angular diameter distances for the redshifts of our targets. In Fig. 11, we show histograms of the physical sizes of the ensemble of cQSOs and rQSOs, and use solid histograms to show the sizes of the extended subset.

The two visually extended cQSOs are the largest systems in our sample, both with sizes $\gtrsim$20 kpc. Two of the extended rQSOs have similar sizes: 0946+2548 and 1153+5651. The three remaining extended rQSOs are only a few kpcs in size, well within the scale of their host galaxies.

While these differences are interesting, it is important to highlight that the majority of the colour-selected QSOs that we have imaged with e-MERLIN remain unresolved at scales of $\lesssim$2 kpc. We interpret this and other results from this work in the following discussion.

4 DISCUSSION

Our studies of the SDSS QSO population (Klindt et al. 2019; Fawcett et al. 2020; Rosario et al. 2020) have conclusively demonstrated that red QSOs (rQSOs) harbour a significantly larger fraction of compact radio sources of moderate radio loudness in comparison to normal blue QSOs (cQSOs). Using e-MERLIN, we have obtained 1.4 GHz (*L*-band) images of sets of MIR luminosity- and redshift-matched rQSOs and cQSOs in a small redshift interval ($1.0 < z < 1.55$) with compact morphologies in the FIRST survey. The new e-MERLIN images achieve angular resolutions of $\approx$0.″2, an improvement of more than an order of magnitude over FIRST, which allows a detailed search for resolved radio structure among the very subpopulation of radio quasars in which rQSOs and cQSOs differ the most.

We undertake Gaussian single- or multi-component decomposition of the radio images of our targets, and apply a battery of tests to search for extended structure: visual assessment, core/beam comparisons, and the examination of positional offsets of the radio core with respect to the optical *Gaia* positions of the QSOs. We also search for differences in the amount of resolved 1.4 GHz emission by comparing FIRST and e-MERLIN fluxes. Our analysis only identifies seven visually extended sources (five rQSOs and two cQSOs) from the final colour-selected subsets; the remaining 32 QSOs are unresolved with e-MERLIN.

In the rest of this discussion, we collate the evidence for morphological differences in the radio structures of red and normal QSOs, and present a plausible scenario that connects the dust that reddens the rQSOs and their radio properties. We also comment broadly on the nature of compact radio sources in QSOs near cosmic noon, as revealed by this e-MERLIN study.

4.1 Kiloparsec-scale radio structures are more common in red QSOs

In terms of the radio structures of the ensemble of QSOs from our study, the clearest result is that the majority of our targets are unresolved and therefore exhibit pure core radio morphologies.

32/40 (82^{+5}_{-8} per cent) of the QSOs remain unresolved at the physical resolution of the e-MERLIN images (1.2–2.5 kpc). Comparisons of the e-MERLIN and FIRST 1.4 GHz fluxes of our targets (Section 3.2) do not indicate the presence of much emission on scales of tens of kpc that may be missed by e-MERLIN.

Of the individual subsamples, 5/19 (26^{+12}_{-7} per cent) of the rQSOs and 2/20 (10^{+11}_{-3} per cent) of the cQSOs are clearly extended. As it stands, our results imply an $\approx 2\sigma$ difference in the incidence of extended structure between the two populations, which we consider to be statistically significant.

Since only a small fraction of the cQSOs show extended structure, our interpretation of the cQSO 1511+3428 is important. For the purposes of baseline statistics, we treat it as a single multicomponent radio source with a nuclear core coincident with the QSO. However, based on the discussion from Section 3.1.7, it is possible that the offset hotspot seen in the image is an independent radio source associated with a neighbouring galaxy. If this were indeed the case, the fraction of cQSOs with extended structure drops to 5^{+9}_{-2} per cent, differing from rQSOs at the $\approx 3\sigma$ level.

At face value, the low incidence of extended radio structures on scales of a few arcseconds among the cQSOs is unexpected. There is no a priori reason that so many QSOs, selected only to be unresolved at >5 arcsec, should not display detectable radio structures between FIRST and e-MERLIN resolutions. For an example of a contrasting result, an early MERLIN survey of Jy-level radio quasars (Reid et al. 1995) only finds one source that remains unresolved at subarcsecond scales, out of a subset of 19 at the same range of redshifts as our e-MERLIN targets.

However, we are unable to identify work in the current literature that offers an unbiased perspective on the high-resolution radio morphologies of QSOs of similar radio luminosities as shown by our targets. The study of Reid et al. (1995) mentioned above, by virtue of its bright radio flux cut, images quasars that are at least

two orders of magnitude more luminous than our sample. A high incidence of bright large-scale lobes is perhaps not surprising in these very powerful systems. Several studies have targeted interesting subsamples, such as those with known large radio jets or steep radio spectra (e.g. Akujor et al. 1991; Lonsdale, Barthel & Miley 1993; Mullin, Riley & Hardcastle 2008), but these have extended radio structure by construction. There have been some high resolution studies of low-redshift and/or radio-quiet QSOs (e.g. Kukula et al. 1998; Jarvis et al. 2019), which typically find extended structures in 50–90 per cent of their sample. However, the targets in these studies are often pre-selected by properties that may be connected to extended radio jets, such as high-velocity outflows in narrow forbidden lines like [O III] λ5007 (e.g. Jarvis et al. 2019).

In this sense, our observations offer a valuable reference for the incidence of extended cm-wave radio structures in typical QSOs hosting low-power radio sources at $z \sim 1$.

4.2 The incidence of radio sources of different sizes among red and normal QSOs

Our e-MERLIN targets were selected as compact or unresolved sources based on images from the FIRST survey. The 5 arcsec angular resolution of FIRST translates to projected sizes of 41–44 kpc at the redshifts of our targets, much larger than the typical sizes of even the massive galaxies that are the likely hosts of these QSOs. As noted above, it is surprising to find that only a few of our QSOs show resolved radio structure in the e-MERLIN images, despite our ability to resolve such structure down to ≈2 kpc and with surface-brightness contrasts of 10–100 s. This implies that radio QSOs show a dearth of emission on scales of several kpcs, approximately in the size range of their host galaxies (e.g. van der Wel et al. 2014).

We investigate this notion further by examining the incidence of radio sources of different (projected) sizes among QSOs in the redshift and radio luminosity ranges of our e-MERLIN targets ($1.0 < z < 1.55$; $10^{25.5} \leq L_{1.4} \leq 10^{26.7}$ W Hz^{-1}). We consider four characteristic physical scales: <2 kpc ('nuclear'), 2–10 kpc ('galactic'),[2] 10–42 kpc ('circumgalactic'), and >42 kpc ('supergalactic').[3]

Our approach is to combine statistics from the FIRST survey and our e-MERLIN programme to evaluate, or place limits on, the fraction of colour-selected QSOs that have radio source sizes within the four ranges defined above. An important detail is that these fractions are evaluated with respect to the entire parent population of coeval colour-selected SDSS QSOs, not just against the radio-detected subsets. This approach normalizes for the key differences in the FIRST radio properties between rQSOs and cQSOs, *viz.* the significantly higher incidence of compact radio sources among rQSOs.

As an illustration, consider the fraction of cQSOs with supergalactic radio sizes. To arrive at this number, we first count cQSOs from the parent sample satisfying our redshift and $L_{1.4}$ cuts that are also resolved by FIRST. We then divide this total by the number of all cQSOs in that redshift range irrespective of radio properties. For the three smaller size bins (nuclear, galactic, and circumgalactic), we bring in constraints from e-MERLIN, which, though limited in statistical size, push well below the FIRST resolution limit. In these cases, we multiply the fraction of cQSOs that are compact in FIRST by the fraction of e-MERLIN targets that have maximum measured sizes at the respective physical scales, propagating uncertainties using binomial statistics (Cameron 2011). Similar calculations are performed in each bin separately for rQSOs and cQSOs, and the results are shown in Fig. 12.

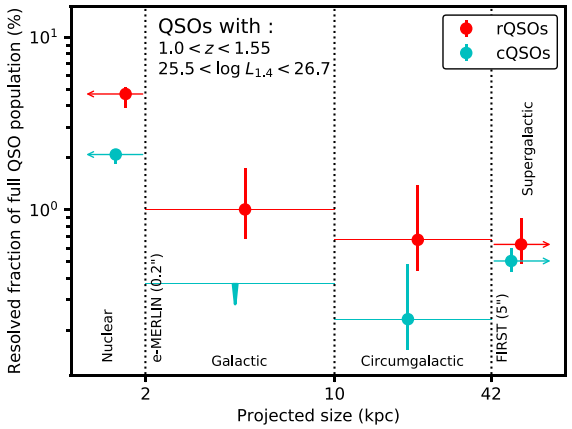

Figure 12. The incidence of radio sources in the $L_{1.4}$ range of our targets with different maximum projected sizes, expressed as a fraction of the respective colour-selected QSO subpopulations from the SDSS DR7 with comparable redshifts. Fractions for the rQSOs (red points) and cQSOs (blue points) are shown separately. See the associated text in Section 4.2 for details.

We first consider the trend shown among cQSOs, which should be representative of normal QSOs of similar redshift and accretion luminosity. Based on the statistics of e-MERLIN targets that remain unresolved, ≈2 per cent of cQSOs contain nuclear low-power core-dominated radio sources. We do not find any cQSOs that have measured e-MERLIN sizes in the 2–10 kpc range, which sets a 2σ upper limit of <0.4 per cent on the fraction on galactic scales. The two e-MERLIN cQSOs that are resolved both have sizes between 10 and 42 kpc, yielding a circumgalactic fraction of 0.1–0.5 per cent. Using the better statistics for the sources resolved by FIRST, the supergalactic fraction settles to 0.5 per cent, comprising of radio galaxies of intermediate radio loudness with traditional FR I/II classifications, as well as more complex extended morphologies (Klindt et al. 2019).

The trend among the rQSOs reveals important differences when contrasted to that of the cQSOs. Klindt et al. (2019) demonstrated that the incidence of FIRST-resolved radio sources among rQSOs is indistinguishable from cQSOs across a broad range of redshifts. Among the QSOs within our working redshift range, the supergalactic fractions for both classes are identical within the statistical errors, confirming this result. However, proceeding towards progressively smaller scales, the fraction of rQSOs rises steadily and deviates strongly from the trends shown by cQSOs. At galactic scales, the three rQSOs that are extended in our e-MERLIN images determine an estimated fraction of ≈1 per cent, more than 2× higher than the conservative upper limit placed on the cQSO fraction. In the nuclear bin, the rQSO incidence is ≈4.5 per cent, again more than 2× the rate found among cQSOs. The significant excess of unresolved radio sources seen among rQSOs from lower resolution surveys (Klindt et al. 2019; Fawcett et al. 2020; Rosario et al. 2020) can be attributed to a truly compact population that lies mostly within the inner few kpcs of their host galaxies. This

[2]The choice of a threshold of 10 kpc to separate galactic and circumgalactic scales is based on the optical sizes of massive galaxies at $z \sim 1.3$, the majority of which are found to be smaller than 10 kpc, with a median effective radius of ≈5 kpc (e.g. van der Wel et al. 2014).

[3]The choice of 42 kpc as a threshold between the circumgalactic and supergalactic scales is set purely by the resolution limit of FIRST projected to our redshifts of interest.

indicates that the likely location of the dust that reddens red QSOs is in the central environment of their AGN.

What can we deduce about the connection between the radio emission and the rQSO phenomenon from these differences in the fractional radio size distributions? The clearest excess among rQSOs is found among resolved and unresolved radio sources at scales $<$10 kpc. From this, we can conclude that the differences cannot be purely associated with the synchrotron population in the immediate vicinity (inner few pcs) of the accretion disc, such as a jet base or corona. At least some of these differences must be driven by a radio-emitting structure that extends beyond the scope of the central engine to explain the differences we find on galactic scales.

4.3 What is responsible for the excess radio emission in red QSOs?

Bringing together various threads from the literature and our own analyses, we explore three potential explanations for the excess radio emission in rQSOs: star formation differences, a higher incidence of small-scale low-power classical radio jets, or widespread nuclear dusty winds.

4.3.1 Star formation

In a popular evolutionary model connecting red and normal QSOs, rQSOs are caught in a special stage during, or shortly after, a powerful merger-sustained starburst event, when an explosive AGN feedback episode is clearing out the gas-rich centre of the host galaxy (e.g. Glikman et al. 2012). Strong differences in the star formation rate (SFR), particularly within the central kpcs, are a natural prediction of this model. Since supernova remnants associated with star formation can produce synchrotron emission at GHz frequencies, could the root of the differences we see in our e-MERLIN images stem from fundamental differences in the SFR and the spatial distribution of star-forming regions in rQSOs?

The compact radio source components in our e-MERLIN images account for almost all of the integrated radio emission in our targets. Even the faintest components that we measure from our images have L-band flux densities $>$0.3 mJy (Table 3), which, at their redshifts, imply $L_{1.4} > 5 \times 10^{24}$ W Hz^{-1}, or SFRs greater than a few 1000 M$_{\odot}$ yr^{-1}, taking well-used calibrations between SFR and $L_{1.4}$ (Murphy et al. 2011; Kennicutt & Evans 2012). Estimates of the SFR from integrated $L_{1.4}$ can be much higher. These derived SFRs are 1–2 orders of magnitude larger than the SFRs of typical QSOs at $z \sim 1$ (Rosario et al. 2013; Stanley et al. 2017; Calistro Rivera et al. 2021). Quite simply, the radio luminosities of our sample are too large for star formation to be an important contributor to the emission we detect with FIRST or e-MERLIN. Even among coeval 'radio-quiet' QSOs, with $L_{1.4}$ fainter than our targets by an order of magnitude, star formation is not found to dominate the integrated 1.4 GHz radio emission (e.g. White et al. 2017). Therefore, we can confidently continue with the notion that the radio differences we see are due to AGN-powered processes.

4.3.2 Jet-powered radio sources

Jet-driven radio galaxies present a plethora of morphologies, and have sizes spanning from nuclear scales to some of the largest coherent structures in the Universe (Miley 1980). Given the long-standing association between radio galaxies and QSOs (Urry & Padovani 1995), it is reasonable to interpret the sources we have

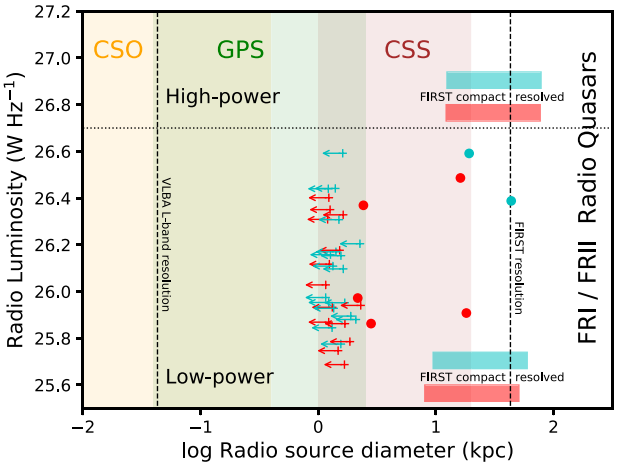

Figure 13. Maximum radio source size versus 1.4 GHz radio power ($L_{1.4}$) for our rQSOs (red points) and cQSOs (cyan points). Filled circles and left-pointing arrows show extended sources and unresolved sources, respectively. The dashed vertical lines mark the typical physical resolution of the FIRST survey and the VLBA at the L band at a characteristic redshift (z) of 1.3. The dotted horizontal line marks a rough transition between low-power and high-power radio sources. The coloured bands spanning the FIRST resolution limit graphically show the relative fractions of radio rQSOs and cQSOs that are determined to be compact or resolved by FIRST. Note that compact sources are more common among rQSOs compared to cQSOs at low radio luminosities, but they are found equally among more luminous systems (e.g. Klindt et al. 2019). We mark using shaded bands the approximate size ranges of the CSS, GPS, and CSO categories of jetted radio sources. The largest extended radio sources, those that are well resolved by FIRST, are the classical double-lobed FRI/II systems.

characterized with e-MERLIN in the context of the population of classical radio galaxies at intermediate redshifts.

The e-MERLIN morphologies of the extended small-scale radio sources in our sample are typically bipolar, but they do not all sport the core/jet or core/lobe structure reminiscent of classical double radio galaxies. However, it is also well known that powerful radio sources that are confined within their hosts often show quite disturbed morphologies on similar size scales (see O'Dea 1998, and references therein). Therefore, morphological information alone is not sufficient to assess their nature.

Additional insight and context come by examining our sources on the space of 1.4 GHz radio luminosity ($L_{1.4}$) versus the maximum physical size in kpc (Fig. 13). Similar diagrams have been employed by earlier studies to explore the dynamical evolution of radio sources (e.g. O'Dea & Baum 1997; Kunert-Bajraszewska et al. 2010; An & Baan 2012; Jarvis et al. 2019).

As jet-powered radio sources evolve, their primary energy loss mechanisms change as they expand and interact with the ambient medium of their host galaxies (see An & Baan 2012, and references therein). Within the dense, approximately constant density interstellar medium of the central few hundreds of pcs of a galaxy, adiabatic losses dominate over synchrotron losses, leading to a low radiative conversion efficiency and a steep radio spectrum. Such sources are called Compact Symmetric Objects (CSOs). As they expand beyond the inner galaxy, the confining gas develops a density gradient decreasing outwards and synchrotron losses catch up to adiabatic losses. A prominent spectral break at cm wavelengths develops and the term Gigahertz-Peaked Spectrum (GPS) is used to describe such sources. As they burst out of their host galaxies, synchrotron losses

take over; jets and lobe expand out into their galactic environment as the spectral break moves to lower frequencies in the form of Compact Steep Spectrum (CSS) sources and eventually the classical doubles of FR I/FR II morphologies.

In Fig. 13, we delineate the ranges of sizes observed in radio galaxies of the various categories outlined above. All these categories can span orders of magnitude in $L_{1.4}$, so we only use their sizes to distinguish them in our diagram, using various shaded regions that none the less have substantial overlap.

The e-MERLIN QSOs that are resolved (circle points) are in the range of sizes shown by CSS sources. This is consistent with their moderately steep meter-wave spectral indices found in our FIRST–TGSS analysis (Fig. 9). The unresolved sources have upper limits to their sizes (left arrow points) that place them in the GPS and CSO regime. If their actual sizes are at the order of hundreds of pc, we expect these objects to predominantly display synchrotron spectra with strong curvature at hundreds of MHz to GHz frequencies (O'Dea & Baum 1997). Unfortunately, from our analysis in Section 3.3, we cannot clearly ascertain whether the meter-wave spectral indices, most of which are limits, suggest a turnover or not, but it is unlikely that the unresolved e-MERLIN sources all show flat or inverted spectra between TGSS and FIRST bands.

4.3.3 *Wind-powered radio sources*

Dusty AGN-driven winds (e.g. Hönig 2019) can also offer an explanation for the small-scale radio emission that we observe. Recently, Calistro Rivera et al. (2021) presented a comparative multiwavelength and spectral analysis of rQSOs and cQSOs selected using the same approach as our earlier works. They report a correlation between the presence of excess hot dust emission in the MIR and strong outflow signatures among rQSOs, which is evidence that dusty winds are responsible for their red colours.

Shocks from fast winds in AGN have been invoked in earlier studies to explain enhanced radio emission in luminous AGNs that also show emission-line outflows (e.g. Zakamska & Greene 2014). The low radio loudness of the excess radio sources in rQSOs is consistent with a possible origin in shocks from AGN-driven winds that also carry enough dust to mildly redden the nuclear spectra in these objects (Rosario et al. 2020).

The radio morphologies produced by such winds are still unclear. They are likely to be bipolar, reflecting the collimation of a wind towards the polar axis of the accretion structure (Williamson, Hönig & Venanzi 2020), but whether they retain their shape over kpcs in the gas-rich environment surrounding the nucleus is subject to debate (Wagner, Umemura & Bicknell 2013). For example, radio-quiet QSOs with strong kpc-scale outflows, systems in which wind shocks are expected to be commonplace, appear to show radio structures that look like classical radio galaxies (Jarvis et al. 2019).

We stress here that it is the *excess* compact radio emission found in rQSOs that we seek to understand. Nuclear radio sources are seen in our cQSOs as well, and these could very well arise from jets or coronal emission since cQSOs are not expected to harbour widespread dusty winds. Since nuclear radio sources are about twice as common among rQSOs as cQSOs (Fig. 12), roughly half of them may arise from standard jet-powered processes. It is the other half, powered by dusty winds, that accounts for the overall enhancement of radio emission in rQSOs in this scenario.

Very long baseline interferometry has the capacity to resolve the small-scale structure of our sources ($<$100 pc). For example, the Very Long Baseline Array (VLBA) has a resolution at 1.4 GHz of 5 mas, probing well into the domain of physical sizes that separate GPS and CSO sources (Fig. 13). Future multifrequency studies with this or complementary facilities may allow us to explore whether the nuclear radio structures in the majority of our targets could be described as the early evolution of bipolar jets.

Another potential test to distinguish between jet-powered or shock-powered explanations is through the use of radio spectral curvature constraints. Jet-driven double radio sources show strong correlations between their spectral turnover frequencies and their source sizes (O'Dea & Baum 1997), a consequence of the dynamic changes that such radio sources undergo as they expand within their host galaxies. Radio structures from wind shocks are not expected to evolve in a similar fashion, and therefore may not lie along such trends.

With multiband GMRT observations that have recently been taken for all 40 e-MERLIN targets (Principal Investigator: V. Fawcett), future work from our team will present a comparative radio spectral and morphological analysis, seeking further insight into the phenomena that fundamentally distinguish red and normal QSOs.

5 CONCLUSIONS

We present e-MERLIN *L*-band images of a sample of 19 red QSOs (rQSOs) and 20 normal QSOs (cQSOs) at redshifts of $1.0 < z < 1.55$. Our targets are matched in redshift and rest-frame 6 μm luminosity ($L_{6\mu m}$), a measure of their nuclear bolometric power, and selected to have moderate 1.4 GHz luminosities ($10^{25.5} \leq L_{1.4} \leq 10^{26.7}$ W Hz^{-1}) and compact morphologies in the FIRST survey (angular resolution of 5 arcsec; $>$40 kpc at the QSO redshifts). The e-MERLIN images resolve radio structures down to $\approx$0.″2, probing host galaxy scales in these QSOs (2–10 kpc).

Following a morphological assessment of the e-MERLIN images, both visually and by means of Gaussian decomposition, we assessed the incidence and distribution of radio sources in our targets across a range of projected size scales. Our main conclusions are as follows:

(i) The majority of both cQSOs and rQSOs have nuclear radio cores that remain unresolved with e-MERLIN (Fig. 3 and Section 4.1).

(ii) We find a statistically significant excess in the incidence of small-scale radio sources (sizes $<$10 kpc) among rQSOs, while confirming that larger radio sources are as common in rQSOs as in cQSOs in the redshift and $L_{1.4}$ range of interest (Section 4.2). We report a very low incidence ($<$0.4 per cent) of sources with galactic-scale sizes (2–10 kpc) among typical QSOs (cQSOs).

(iii) Incorporating TGSS constraints, most of the sources with extended e-MERLIN structure also show typical steep radio spectral indices (Section 3.3).

(iv) Unlike the cQSOs, rQSOs with extended e-MERLIN emission tend to be of intermediate radio loudness (Section 3.4).

(v) We consider various scenarios to explain the excess in kpc-scale radio structures we find among rQSOs. Current constraints from radio morphologies and spectral indices imply that the differences cannot arise purely from the accretion structure (the accretion disc and/or corona), but must entail differences in components that partially extend out into the host galaxy. These could be either classical jet-powered radio sources or those powered by winds. Since the key feature that defines rQSOs is the presence of moderate dust extinction towards their nuclei, we postulate that dusty winds are widespread among rQSOs, and the shocks that these winds drive into the interstellar medium of their host galaxies are responsible for the particular radio properties of red QSOs.

ACKNOWLEDGEMENTS

We thank the anonymous referee for input that has improved the material and message of this work. DJR and DMA acknowledge support from the UK Science and Technology Facilities Council (STFC) through ST/T000244/1. JM acknowledges financial support from the State Agency for Research of the Spanish Ministry of Science, Innovation and Universities (MCIU) through the 'Center of Excellence Severo Ochoa' award to the Instituto de Astrofísica de Andalucía (SEV-2017-0709) and from the grant RTI2018-096228-B-C31 (MICIU/FEDER, EU). e-MERLIN is a National Facility operated by the University of Manchester at Jodrell Bank Observatory on behalf of STFC, part of UK Research and Innovation. Funding for the SDSS and SDSS-II has been provided by the Alfred P. Sloan Foundation, the Participating Institutions, the National Science Foundation, the U.S. Department of Energy, the National Aeronautics and Space Administration, the Japanese Monbukagakusho, the Max Planck Society, and the Higher Education Funding Council for England. This work has made use of data from the European Space Agency (ESA) mission *Gaia* processed by the *Gaia* Data Processing and Analysis Consortium (DPAC). Funding for the DPAC has been provided by national institutions, in particular the institutions participating in the *Gaia* Multilateral Agreement.

DATA AVAILABILITY

The e-MERLIN data used in this work are available from the corresponding author on reasonable request. All other data are in the public domain and accessible through the corresponding data archives. All measurements required to replicate our results are made available in this paper in the form of figures and tables.

REFERENCES

Akujor C. E., Spencer R. E., Zhang F. J., Davis R. J., Browne I. W. A., Fanti C., 1991, MNRAS, 250, 215
An T., Baan W. A., 2012, ApJ, 760, 77
Becker R. H., White R. L., Helfand D. J., 1995, ApJ, 450, 559
Benn C. R., Vigotti M., Carballo R., Gonzalez-Serrano J. I., Sanchez S. F., 1998, MNRAS, 295, 451
Best P. N., Heckman T. M., 2012, MNRAS, 421, 1569
Calistro Rivera G. et al., 2021, A&A, 649, A102
Cameron E., 2011, Publ. Astron. Soc. Aust., 28, 128
Fawcett V. A., Alexander D. M., Rosario D. J., Klindt L., Fotopoulou S., Lusso E., Morabito L. K., Calistro Rivera G., 2020, MNRAS, 494, 4802
Fitzpatrick E. L., 1999, PASP, 111, 63
Francis P. J., Drake C. L., Whiting M. T., Drinkwater M. J., Webster R. L., 2001, Publ. Astron. Soc. Aust., 18, 221
Gaia Collaboration, 2018, A&A, 616, A1
Georgakakis A., Clements D. L., Bendo G., Rowan-Robinson M., Nandra K., Brotherton M. S., 2009, MNRAS, 394, 533
Glikman E. et al., 2012, ApJ, 757, 51
Glikman E., Gregg M. D., Lacy M., Helfand D. J., Becker R. H., White R. L., 2004, ApJ, 607, 60
Helfand D. J., White R. L., Becker R. H., 2015, ApJ, 801, 26
Hönig S. F., 2019, ApJ, 884, 171
Intema H. T., Jagannathan P., Mooley K. P., Frail D. A., 2017, A&A, 598, A78
Ivezić Ž. et al., 2002, AJ, 124, 2364
Jarvis M. E. et al., 2019, MNRAS, 485, 2710
Kennicutt R. C., Evans N. J., 2012, ARA&A, 50, 531
Kim D., Im M., 2018, A&A, 610, A31
Klindt L., Alexander D. M., Rosario D. J., Lusso E., Fotopoulou S., 2019, MNRAS, 488, 3109
Kukula M. J., Dunlop J. S., Hughes D. H., Rawlings S., 1998, MNRAS, 297, 366
Kukula M. J., Dunlop J. S., McLure R. J., Miller L., Percival W. J., Baum S. A., O'Dea C. P., 2001, MNRAS, 326, 1533
Kunert-Bajraszewska M., Gawroński M. P., Labiano A., Siemiginowska A., 2010, MNRAS, 408, 2261
Lonsdale C. J., Barthel P. D., Miley G. K., 1993, ApJS, 87, 63
Miley G., 1980, ARA&A, 18, 165
Mullin L. M., Riley J. M., Hardcastle M. J., 2008, MNRAS, 390, 595
Murphy E. J. et al., 2011, ApJ, 737, 67
O'Dea C. P., 1998, PASP, 110, 493
O'Dea C. P., Baum S. A., 1997, AJ, 113, 148
Pei Y. C., 1992, ApJ, 395, 130
Planck Collaboration XIII, 2016, A&A, 594, A13
Podigachoski P. et al., 2015, A&A, 575, A80
Rakshit S., Stalin C. S., Kotilainen J., 2020, ApJS, 249, 17
Reid A., Shone D. L., Akujor C. E., Browne I. W. A., Murphy D. W., Pedelty J., Rudnick L., Walsh D., 1995, A&AS, 110, 213
Richards G. T. et al., 2002, AJ, 123, 2945
Richards G. T. et al., 2003, AJ, 126, 1131
Rosario D. J. et al., 2013, A&A, 560, A72
Rosario D. J., Fawcett V. A., Klindt L., Alexand er D. M., Morabito L. K., Fotopoulou S., Lusso E., Calistro Rivera G., 2020, MNRAS, 494, 3061
Rose M., Tadhunter C. N., Holt J., Rodríguez Zaurín J., 2013, MNRAS, 432, 2150
Schneider D. P. et al., 2010, AJ, 139, 2360
Smolčić V., 2009, ApJ, 699, L43
Stanley F. et al., 2017, MNRAS, 472, 2221
Tsai A. L., Hwang C. Y., 2017, ApJ, 842, 57
Urry C. M., Padovani P., 1995, PASP, 107, 803
van der Wel A. et al., 2014, ApJ, 788, 28
Wagner A. Y., Umemura M., Bicknell G. V., 2013, ApJ, 763, L18
Webster R. L., Francis P. J., Petersont B. A., Drinkwater M. J., Masci F. J., 1995, Nature, 375, 469
White R. L., Helfand D. J., Becker R. H., Gregg M. D., Postman M., Lauer T. R., Oegerle W., 2003, AJ, 126, 706
White R. L., Helfand D. J., Becker R. H., Glikman E., de Vries W., 2007, ApJ, 654, 99
White S. V., Jarvis M. J., Kalfountzou E., Hardcastle M. J., Verma A., Cao Orjales J. M., Stevens J., 2017, MNRAS, 468, 217
Williamson D., Hönig S., Venanzi M., 2020, ApJ, 897, 26
Young M., Elvis M., Risaliti G., 2008, ApJ, 688, 128
Zakamska N. L., Greene J. E., 2014, MNRAS, 442, 784

SUPPORTING INFORMATION

Supplementary data are available at *MNRAS* online.

Figure S1. Visualizations of the single-component Gaussian fits to the e-MERLIN images of QSOs that were determined to have unresolved cores.
Figure S2. Visualizations of the multicomponent Gaussian fits to the e-MERLIN images of QSOs that were visually determined to be resolved.

Please note: Oxford University Press is not responsible for the content or functionality of any supporting materials supplied by the authors. Any queries (other than missing material) should be directed to the corresponding author for the article.

This paper has been typeset from a TEX/LATEX file prepared by the author.